

# Relaxation Dynamics of Entangled Linear Polymer Melts via Molecular Dynamics Simulations

Alireza F. Behbahani<sup>1,\*</sup> and Friederike Schmid<sup>1,†</sup>

<sup>1</sup>*Institut für Physik, Johannes Gutenberg-Universität Mainz, Staudingerweg 7, D-55099 Mainz, Germany*

## Abstract

We present an extensive analysis of the relaxation dynamics of entangled linear polymer melts via long-time molecular dynamics simulations of a generic bead-spring model. We study the mean-squared displacements, the autocorrelation function of the end-to-end vector,  $P(t)$ , the single-chain dynamic structure factor,  $S(q, t)$ , and the linear viscoelastic properties, especially the shear stress relaxation modulus,  $G(t)$ . The simulation data are compared with the theoretically expected scaling laws for different time regimes of entangled melts, and with analytical expressions that account for different relaxation mechanisms in the tube model, namely, reptation, contour length fluctuation (CLF), and constraint release (CR). CLF involves a  $t^{1/4}$  scaling regime in the time-dependence of  $(1 - P(t))$ . With increasing chain length, a gradual development of this scaling regime is observed. In the absence of CR, the tube model further predicts that at long times, the chain dynamics is governed by one central quantity, the “surviving tube fraction”  $\mu(t)$ . As a result, one expects  $S(q, t) \propto G(t) \propto P(t)$  in that time regime. We test this prediction by comparing  $S(q, t)$  and  $G(t)$  with  $P(t)$ . For both quantities, proportionality with  $P(t)$  is not observed, indicating that CR has an important effect on the relaxation of these two quantities. Instead, to a very good approximation, we find  $G(t) \propto P(t)^2$  at late times, which is consistent with the dynamic tube dilation or double reptation approximations for the CR process. In addition, we calculate non-local mobility functions, which can be used in dynamic density functional theories for entangled inhomogeneous polymer blends, and discuss the effect of entanglements on the shape of these functions.

## I. INTRODUCTION

The simplest basic model of linear polymer dynamics, the Rouse model, describes a single Gaussian bead-spring chain that performs unrestricted Brownian movement in a viscous medium. This simple model does not capture the dynamics of long polymers in a melt because chains cannot cross each other, and therefore the surrounding chains strongly restrict the movement of a target chain. To account for this, Edwards, de Gennes, and Doi proposed the so-called tube model, which replaces the effect of the surrounding chains by a confining tube along the contour of the target chain [1, 2]. The tube restricts the displacement of monomers perpendicular to the local axis of the tube, to a distance called tube diameter, but the motion of the chain along the contour of the tube is not restricted. In the basic tube model, the curvilinear diffusive motion of the chain along the tube, called reptation, is assumed to be the (only) mechanism by which the chain escapes from the tube and adopts a new conformation [1–3]. However, it is well-known that the pure reptation mechanism cannot quantitatively explain various features of entangled polymer melt dynamics, such as the scaling exponents of the zero-shear viscosity and the diffusion coefficient as a function of chain length [3, 4].

To describe polymer melt dynamics more quantitatively, two additional relaxation mechanisms have been taken into account. The first mechanism is contour length fluctuation (CLF), which takes into account incoherent chain movements inside the tube (movements other than reptation, which is the chain’s coherent curvilinear motion). CLF causes part of the chain to exit the tube at short

times and reduces the effective distance that the chain needs to travel via reptation to completely escape from the tube [3–5]. The incorporation of CLF into the tube model significantly modifies its predictions. In particular, the combination of reptation and CLF predicts that, over a wide range of molecular weights, the viscosity scales approximately as  $N^{3.4}$  and the diffusion coefficient as  $N^{-2.4}$  with the chain length  $N$ , in agreement with experimental findings [4, 6]. The second additional relaxation mechanism is constraint release (CR), which originates from the motion of the surrounding chains that form the confining tube for the target chain. It is often assumed that the relaxation of a surrounding chain leads to a local reorganization (or a local jump) of the tube, but the tube diameter is not perturbed. Even though some chains no longer contribute to the tube, others come in and impose new constraints, such that the average structure of the melt is conserved. The local rearrangements of the tube due to CR events lead to a slow Rouse-like motion of the tube, and this Rouse-like motion can contribute to the relaxation of the chain [3, 4, 7, 8]. It is worth mentioning that apart from this “Rouse-tube” model, the CR mechanism has also been viewed as a process that increases the effective tube diameter with time, *i.e.*, leads to dynamic tube dilation [9, 10].

Molecular dynamics simulations have proven to be efficient tools for studying the dynamics of entangled polymer melts and for testing the predictions of the tube model. For example, the tube model predicts a series of scaling regimes for the mean-squared displacement of monomers,  $g_1(t)$ , and chain center-of-mass,  $g_3(t)$ , with time. In particular, it predicts an early time regime where  $g_1(t)$  and  $g_3(t)$  scale as  $g_1(t) \sim t^{1/4}$  and  $g_3(t) \sim t^{1/2}$ , due to the restricted Rouse motion of the chain inside the tube. These scaling regimes, or signs of the gradual development of these regimes upon increasing chain length, have been observed in several simulations of coarse-grained bead-

\* aforooza@uni-mainz.de

† friederike.schmid@uni-mainz.de

spring or chemistry-specific models [11–22]. The chain length-dependence of the diffusion coefficient and the zero shear viscosity have also been investigated using simulations, and the transition from unentangled Rouse-like behavior to entangled behavior has been detected [21–26]. Few simulation works have studied the single-chain dynamic structure factor,  $S(q, t)$ , of entangled polymer melts [11, 12, 24, 27]. This dynamical observable is experimentally accessible, *e.g.*, using the neutron spin echo technique [28–31]. The tube model predicts a fast partial decay of  $S(q, t)$  due to local motions of the chain inside the tube followed by a slow long-time decay due to escaping from the tube [28, 32]. The Time-scale separation between these two processes leads to the appearance of a plateau-like regime in the  $S(q, t)$  curve, which has been observed in molecular dynamics simulations [27]. The viscoelastic properties of entangled polymer melts, which have been studied in detail experimentally [33–36] and are essential for the applications of polymers, have also been calculated in simulation [13, 14, 19, 21, 22, 37–40]. In particular, Likhtman *et al.* [14] calculated the shear stress relaxation modulus,  $G(t)$ , of bead-spring polymer models over a rather wide range of chain lengths, from unentangled to moderately entangled chains. The overall relaxation of polymer chains can be directly studied by analyzing the dynamics of the end-to-end vector, quantified through  $P(t)$ , the autocorrelation function of the end-to-end vector. This quantity is related to the dielectric relaxation spectra of the so-called type A polymers that have dipole moments along the chain backbone [41–43]. Despite providing direct information about the relaxation of the chains, this quantity has not been extensively studied using simulations. Single-chain slip-spring models, with the capability of adjusting CR parameters, have been used to study the effect of CR environment on the dynamics of the end-to-end vector [44, 45]. More recently, using a multiscale approach (with a multi-chain slip-spring model at the coarsest level of description), it has been reported that the pure reptation model can not describe the dynamics of long polyisoprene chains [22]. Note that single-chain or multi-chain slip-spring models are coarse-grained and computationally efficient models that do not strictly prevent chain crossings, but mimic entanglement effects by a set of springs that restrict the lateral movements of the chain [46–54].

The present work complements and goes beyond the previous contributions in several aspects: (i) We provide a detailed joint analysis of various quantities that characterize the chain dynamics: the autocorrelation function of the end-to-end vector,  $P(t)$ , the single-chain dynamic structure factor,  $S(q, t)$ , the linear viscoelastic properties, characterized by  $G(t)$ , and the mean-squared displacements. This is done for a wide range of molecular weights ranging from the unentangled to entangled regimes through long-time molecular dynamics simulations up to the terminal time. The data of  $S(q, t)$  are also used for the calculation of non-local mobility functions, that can be used in investigating the dynamics of structure development in

heterogeneous polymer melts. (ii) We discuss different relaxation processes and analyze their signatures. To directly detect the signatures of CLF, we mainly analyze  $P(t)$  and compare its behavior with that of  $g_1(t)$ . To detect the signatures of CR, different dynamical observables are compared with each other. A central quantity in this analysis is the “surviving tube fraction”  $\mu(t)$ , a fundamental quantity in the tube model, which denotes the fraction of the (primitive) chain that still remains in the original tube formed at  $t = 0$ . In the absence of CR (*i.e.*, assuming a fixed tube in space), the tube model predicts a relation  $S(q, t) \propto G(t) \propto P(t) = \mu(t)$  [4, 32, 41] at late times  $t$ . It reflects the fact that, in the absence of CR, the behavior of these quantities should be governed by the process of escaping from the tube, as quantified by  $\mu(t)$ . We note that the correlation between different dynamical properties has also been investigated in experimental works, particularly using parallel rheology and dielectric relaxation spectroscopy techniques [41, 55]. (iii) We perform a detailed comparison of the simulation results with theoretical expressions based on different relaxation mechanisms. The  $P(t)$  and  $S(q, t)$  data are compared with the predictions of the pure reptation model and the combination of reptation and CLF. The  $G(t)$  data are compared with the predictions of the Likhtman-McLeish model [56] which considers reptation, CLF, and CR mechanisms. The latter discussion is similar in spirit to one in a previous study by Hou *et al.* [37], however, our approach is different and the results confirm a simple relation between  $G(t)$  and  $P(t)$ .

The manuscript is organized as follows: In the next section, we introduce the model used for the simulations. Then, we analyze mean-squared displacements, dynamics of the end-to-end vector, single-chain dynamic structure factor, and linear viscoelastic properties, respectively. Finally, in the last section, we summarize the results.

## II. MODEL

Molecular dynamics simulations have been performed with the standard fully flexible Kremer-Grest bead-spring model [11]. In this model, all beads have mass  $m$  and purely repulsive non-bonded interactions described by the Weeks-Chandler-Anderson potential [57] with characteristic length scale  $\sigma$  and prefactor  $\varepsilon$ . The bond-stretching interactions are given by a FENE potential that prevents chain crossing and no angle-bending potential is applied. All quantities are expressed in units  $\sigma$ ,  $\varepsilon$ , and  $m$ , *e.g.*, the basic time unit is  $\tau = \sqrt{m\sigma^2/\varepsilon}$ . The bead density is equal to  $\rho = 0.85\sigma^{-3}$ . Simulations were carried out at  $k_B T = 1\varepsilon$  using a Langevin thermostat, with bead friction  $0.5\tau^{-1}$ , and a time step  $dt = 0.01\tau$  was used for integrating the equations of motion using the LAMMPS package [58]. Simulations were performed for a wide range of chain lengths  $N$ , *i.e.*,  $N = 5, 10, 20, 30, 50, 100, 150, 200, 400$ , and 1000 (the results for  $N = 5$  and 20 are reported in few cases). For these values of  $N$ , the simu-

lation box contained 4800, 2400, 500, 800, 400, 400, 400, 192 and 216 chains, respectively. Depending on  $N$ , production runs were carried out for around  $10^5\tau$  up to  $10^8\tau$  ( $10^7$  to  $10^{10}$  time steps). In most cases, the initial pre-equilibrated configurations for the simulations were taken from previous simulations of melts of a chemistry-specific coarse-grained model [21]. After converting the units and adjusting the melt density to  $\rho = 0.85\sigma^{-3}$ , these systems were subjected to long-time equilibration runs. To confirm that the resulting structures were equilibrated, we measured the internal distances of the model chains, shown in Fig. 1. This figure shows  $R^2(n)/n$  versus  $n$ , where  $R^2(n)$  is the mean-squared distance between the two monomers separated by  $n$  bonds along a chain. For large  $n$ ,  $R^2(n)/n$  tends to a constant value and does not have significant fluctuations, as expected for the random-walk structure of the chains at large scales.

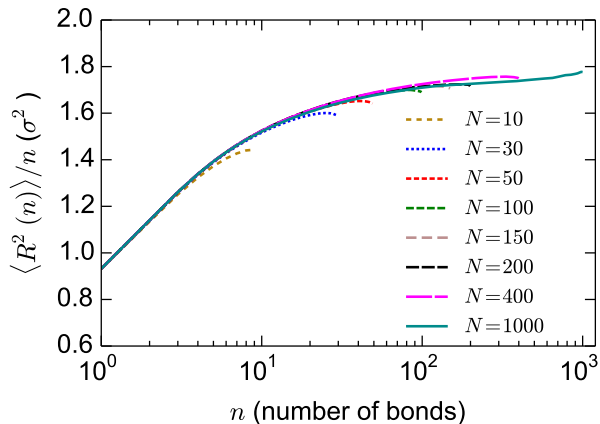


FIG. 1. Mean-squared internal distances of the simulated chains.  $R^2(n)$  is the mean-squared distance between two monomers separated by  $n$  bonds along a chain.

Based on the size of the chains with length  $N \geq 200$ , we estimate the effective segment size to be  $b = 1.32\sigma$ , using  $R_{ee}^2 = (N-1)b^2$ , where  $R_{ee}^2$  is the mean-squared end-to-end distance of a chain containing  $N$  beads. Also, we estimate the Kuhn length to be  $l_k = 1.81\sigma$ , using  $R_{ee}^2 = N_k l_k^2$  and  $R_{max} = N_k l_k$  where  $R_{max} = (N-1)l_b$  is the contour length of the chain. Here,  $l_b = 0.965\sigma$  is the average bond length between two consecutive beads along a chain. For Kremer-Grest chains with length  $N > 100$ , the monomeric friction coefficient has been previously calculated from the relaxation of the large Rouse modes, giving  $\zeta = 25\tau^{-1}$  [11, 20, 59, 60]. Also, through the primitive path analysis [61], the entanglement length of large model chains has been estimated to be close to  $N_{e,ppa} = 87$ [62, 63]. The entanglement length is related to the plateau modulus  $G_N^0$  via  $G_N^0 = \frac{4}{5}\rho k_B T / N_e$ . The value of the plateau modulus has been estimated by Likhtman *et al.* [14] from the simulation of a single-chain slip-link model parameterized based on the bead-spring model utilized in this work, giving  $G_N^0 = 0.013 \varepsilon / \sigma^3$  corresponding to  $N_e = 52$ . As we will discuss in detail in Section III D, this value also provides a consistent description

of the plateau modulus in the present simulations. Given this latter estimate of  $N_e$ , the step length of the tube (or distance between entanglements along one chain), which can be calculated from the end-to-end distance of a sub-chain of length  $N_e$  segments, equals  $N_e b^2 = 9.52\sigma$ . In the current work, the tube diameter,  $a$ , is assumed [28, 56] to be equal to the step length of the tube.

### III. RESULTS AND DISCUSSION

#### A. Mean-squared displacements

An initial overview of different dynamical regimes in the system can be obtained by inspecting the average mean-squared displacement of monomers (beads),  $g_1(t)$ , and the average mean-squared displacements of the centers-of-mass of the chains,  $g_3(t)$ :

$$\begin{aligned} g_1(t) &= \langle [\mathbf{r}(t) - \mathbf{r}(0)]^2 \rangle, \\ g_3(t) &= \langle [\mathbf{r}_{CM}(t) - \mathbf{r}_{CM}(0)]^2 \rangle. \end{aligned} \quad (1)$$

Here  $\langle \rangle$  denotes averaging over all target monomers/chains and time origins in a trajectory.

Both  $g_1(t)$  and  $g_3(t)$  exhibit different behaviors in unentangled and entangled melts. For unentangled melts, the Rouse model predicts the following scaling regimes in the limit of long chains [2]:

$$g_1(t) \sim \begin{cases} t^1 & t < \tau_0 & \text{(I}_R) \\ t^{\frac{1}{2}} & \tau_0 < t < \tau_R & \text{(II}_R) \\ t^1 & t > \tau_R & \text{(III}_R) \end{cases}, \quad (2)$$

where  $\tau_0 = \zeta b^2 / (3\pi^2 k_B T)$  is a monomeric time and  $\tau_R = \tau_0 N^2$  is the Rouse time of the chain. For entangled melts, the tube model predicts the following regimes (in the absence of CR) [2, 3, 11]:

$$g_1(t) \sim \begin{cases} t^1 & t < \tau_0 & \text{(I)} \\ t^{\frac{1}{2}} & \tau_0 < t < \tau_e & \text{(II)} \\ t^{\frac{1}{4}} & \tau_e < t < \tau_R & \text{(III)} \\ t^{\frac{1}{2}} & \tau_R < t < \tau_d & \text{(IV)} \\ t^1 & t > \tau_d & \text{(V)} \end{cases}, \quad (3)$$

where  $\tau_e = \tau_0 N_e^2$  is the entanglement time,  $\tau_R = \tau_0 N^2$  is the Rouse time, and  $\tau_d \sim N^\alpha$  is the disentanglement time of the chain, where  $\alpha \approx 3.4$  over a wide range of chain lengths (based on the reptation and CLF mechanisms [4]). At time scales shorter than  $\tau_e$  the chains do not feel the entanglements, and perform unrestricted Rouse motion. After  $\tau_e$  the monomers are constrained to move along their confining tubes. In the range of  $\tau_e < t < \tau_R$  the chain performs restricted incoherent Rouse motion, and in the range of  $\tau_R < t < \tau_d$ , coherent diffusion inside the tube. Because of the random-walk structure of the tube, these exponents are half of the normal Rouse exponents (Eq. (2)). After  $\tau_d$ , when the chains fully escape from their

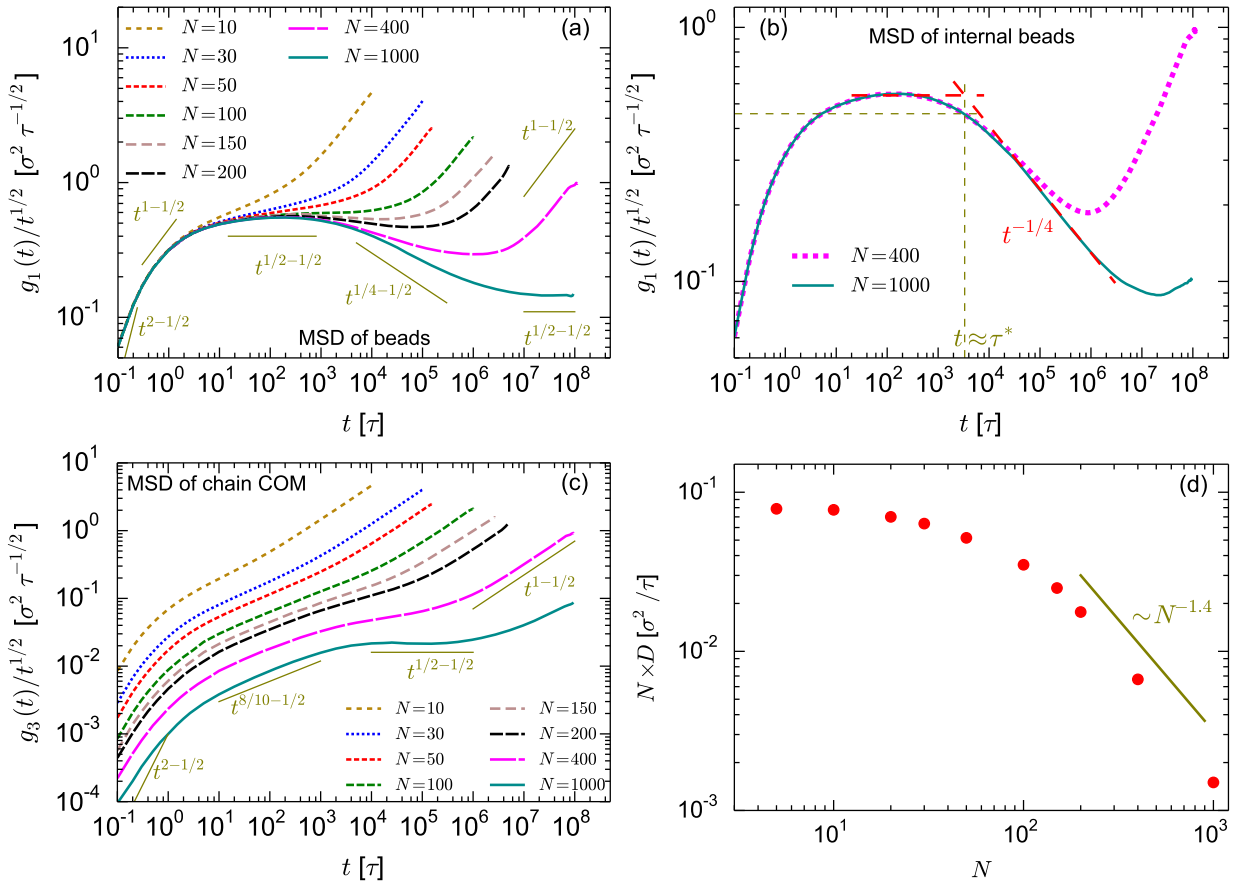


FIG. 2. (a) Mean-squared displacement of all monomers normalized with  $t^{1/2}$ . (b) Mean-squared displacement of the internal monomers normalized with  $t^{1/2}$ . For  $N = 400$  and  $1000$ , averaging has been performed over 25 and 100 internal monomers respectively. (c) Mean-squared displacement of the centers-of-mass of the chains divided by  $t^{1/2}$ . (d)  $DN$  vs.  $N$  where  $D$  is the self-diffusion coefficient of the chains calculated from the long-time behavior of  $g_3(t)$ .

confining tubes,  $g_1(t)$  shows normal diffusive behavior. In the following, we will label these different time regimes as regime I-V as indicated in Eq. (3). Different regimes in the Rouse case are denoted  $\text{I}_R$ ,  $\text{II}_R$ , and  $\text{III}_R$ , see Eq. (2).

Fig. 2a shows the chain length dependence of  $g_1(t)$ , calculated by averaging over all monomers, including chain ends. To better illustrate deviations from the Rouse behavior,  $g_1(t)$  is divided by the Rouse slope,  $t^{1/2}$  (characterizing the regimes  $\text{II}_R$  and  $\text{II}$ ). At very short times, a nearly ballistic regime ( $g_1(t) \sim t^2$ ) is observed. This regime reflects the inertia of monomers and is not present in the Equations (2) and (3), which are based on models for overdamped Brownian motion. In the Lennard-Jones units, the transition from underdamped to overdamped motion is expected around  $t \approx 1\tau$ . At very late times,  $g_1(t)$  reflects normal diffusive behavior ( $g_1(t) \sim t$ ) with the diffusion constant of the whole chain. At intermediate times, different regimes are observed depending on the length of the chain. The  $g_1(t)$  of short chains ( $N < 100$ ) always grows faster than  $t^{1/2}$  before reaching normal diffusion. This can be attributed to the finite length of the chains. Indeed, the Rouse model for short chains

(finite number of Rouse modes) also predicts exponents larger than  $1/2$  [21]. For  $N \leq 100$ ,  $g_1(t)/t^{1/2}$  has positive or zero slopes before the normal diffusion regime, but for  $N > 100$ , an interval of negative slope (in a double logarithmic plot) gradually emerges, which is a characteristic of entangled dynamics. With increasing chain length  $N$ , the negative slope becomes gradually more pronounced and approaches the prediction of the tube model,  $g_1(t)/t^{1/2} \sim t^{-1/4}$  (regime  $\text{III}$  in Eq. (3)).

Among all monomers, the behavior of  $g_1(t)$  for middle monomers in a chain is expected to come closest to the prediction of the tube model [11]. Therefore, Fig. 2b shows separately the function  $g_1(t)$  of middle monomers for chains of length  $N = 400$  and  $N = 1000$  (averaged over 25 and 100 middle monomers, respectively). As expected, the transition between scaling regimes is much more pronounced, and for  $N = 1000$ , a  $t^{1/4}$  regime can clearly be seen. Based on these data, the early  $t^{1/2}$  and the  $t^{1/4}$  regimes intersect, approximately, at time  $\tau^* = 3320\tau$  and  $g_1(\tau^*) = 26.3\sigma^2$ . For the estimation of the intersection time, we determine the intersection between the two tangent lines corresponding to the  $t^{1/2}$  and the

$t^{1/4}$  regimes in a double logarithmic plot as shown in Fig. 2b (dashed red lines). We note that the transition between different regimes is continuous and therefore the determination of the transition time has a degree of uncertainty. The transition point can be used for roughly estimating the entanglement time  $\tau_e$  and the tube diameter  $a$  (assuming  $a^2 = N_e b^2$ ) [11, 12, 15, 18, 20, 38, 56, 64]. Different expressions have been put forward in the literature. Kremer and Grest [11] assumed  $\tau_e = \tau^*$  and  $g_1(\tau^*) = 2R_g^2(N_e) = a^2/3$ . These relations give  $\tau_e = 3320\tau$  and  $a = 8.9\sigma$ . From the values of  $\tau_e$  or  $a$ , one can also estimate the entanglement length  $N_e$  via the relations  $a^2 = N_e b^2$  or  $\tau_e = \tau_0 N_e^2$  quoted earlier. Therefore, the above values of  $\tau_e$  and  $a$  correspond to  $N_e = 48$  and  $N_e = 45$ , respectively. These estimates of  $N_e$  are consistent with each other and also are close to  $N_e = 52$ , corresponding to the plateau modulus. Likhtman and McLeish [56] also proposed expressions close to those mentioned above. More recently, Hou [64] suggested to use  $\tau_e = 9\tau^*/\pi$  and  $g^* = 2/(3\pi)a^2$ , where  $g^*$  (which is slightly different from  $g_1(\tau^*)$ ) is taken from the intersection point of the tangent lines on the  $g_1(t)$  curves (red dashed lines in Fig. 2b). These relations give  $\tau_e = 9516\tau$  and  $a = 12.1\sigma$ . These values of  $\tau_e$  and  $a$  correspond to  $N_e = 80$  and  $N_e = 84$ , which are larger than the above estimates based on the suggestion of Kremer and Grest. Similar values have been reported previously [64]. We summarize these rough estimates of  $N_e$ , calculated based on  $g_1(t)$ , in Table I. This table also contains the  $N_e$  values calculated based on the plateau modulus and primitive path analysis, and the  $N_e$  values used for the description of the simulation data based on theoretical models, as discussed in other sections.

Quantity/method	$N_e$	$a = \sqrt{N_e}b$	$\tau_e = \tau_0 N_e^2$
Plateau modulus [14] (Section III D)	52	$9.5\sigma$	$4.0 \cdot 10^3 \tau$
Primitive path analysis [62, 63]	87	$12.3\sigma$	$11 \cdot 10^3 \tau$
$g_1(t)$ (Section III A)			
$\tau_e = \tau^*$	48		$*3.3 \cdot 10^3 \tau$
$a^2 = 3g_1(\tau^*)$ [11]	45	$*8.9\sigma$	
$\tau_e = 9\tau^*/\pi$	80		$*9.5 \cdot 10^3 \tau$
$a^2 = 3\pi g^*/2$ [64]	84	$*12.1\sigma$	
$P(t)$ (Section III B), Eq. 9	52		
$S(q, t)$ (Section III C)			
Pure reptation, Eq. (11 & 13)	156	$16.5\sigma$	
CLF, Eq. (11 & 14)	100	$13.3\sigma$	

TABLE I. Summary of the  $N_e$  values calculated based on the plateau modulus, primitive path analysis, and monomeric mean-squared displacements ( $g_1(t)$ ), together with the  $N_e$  values used for the description of the measured  $P(t)$  and  $S(q, t)$  data based on the theoretical models. The corresponding values of the tube diameter,  $a$ , and entanglement time,  $\tau_e$ , are also shown in some cases. In the case of  $g_1(t)$ , the stars mark the quantities estimated directly from the simulation data. The relations between  $N_e$ ,  $a$ , and  $\tau_e$  are shown in the table. We use these relations with  $b = 1.32\sigma$ ,  $\zeta = 25\tau^{-1}$ , and  $\tau_0 = \zeta b^2 / (3\pi^2 k_B T) = 1.47\tau$  for the effective segment size, the monomeric friction coefficient, and the monomeric time, respectively.

Next, we consider the chain length dependence of  $g_3(t)$ , shown in Fig. 2c. As before, the curves are divided by  $t^{1/2}$  to better illustrate the transition between different scaling regimes. The tube model predicts the following regimes for the behavior of  $g_3(t)$  of entangled chains [4, 11]:

$$g_3(t) \sim \begin{cases} t^1 & t < \tau_e \\ t^{1/2} & \tau_e < t < \tau_R \\ t^1 & t > \tau_R \end{cases} . \quad (4)$$

The sub-diffusive  $t^{1/2}$  regime (corresponding to the  $t^{1/4}$  regime of  $g_1(t)$ ) is important because it is not present in the  $g_3(t)$  of unentangled Rouse chains. As shown in Fig. 2c, upon increasing chain length, a plateau region, corresponding to the  $t^{1/2}$  regime of  $g_3(t)$ , gradually emerges in the  $g_3(t)/t^{1/2}$  curves. For  $N = 1000$ , a fully developed plateau is observed, in agreement with the theoretical prediction. The short-time behavior of  $g_3(t)$  is also worth attention. After the initial nearly ballistic regime, all  $g_3(t)$  curves evolve almost with  $t^{0.8}$ , which is different from the theoretically expected  $t^1$  scaling. This behavior has already been observed previously and was attributed to the inter-molecular interactions, which are ignored in the Rouse model [65]. Figure S1 in Supporting Information (SI) shows  $g_3(t)$  divided by  $t^{0.8}$ . In such a presentation, the gradual development of the  $t^{1/2}$  regime for the entangled chains appears as the gradual development of a region with a negative slope. In line with the behavior of  $g_1(t)/t^{1/2}$ , a negative slope of  $g_3(t)/t^{0.8}$  is seen for  $N > 100$ .

Fig. 2d shows  $ND$  vs.  $N$ , where  $D$  is the self-diffusion coefficient of the chains calculated from the long-time diffusive regime of  $g_3(t)$ , using  $g_3(t) = 6Dt$ . In the simulation window, the behavior of  $g_3(t)$  for the chain length  $N = 1000$  comes close to the normal diffusion regime ( $g_3(t)$  reaches values around  $3R_g^2$  during the simulation time). For shorter chains with length  $N < 1000$ , normal diffusion is clearly observed at late times. Therefore, overall, reasonable measurements of  $D$  can be performed. Note that, besides the chain lengths given in Fig. 2c, the diffusion coefficients for  $N = 5$  and 20 are also included in Fig. 2d. The Rouse scaling,  $D \sim N^{-1}$ , is seen in the neighborhood of the shortest chain lengths under consideration here. A similar behavior has been observed previously [11]. Note that, deviations from the Rouse behavior were reported [21, 22] in simulations of chemistry-specific unentangled melts; in those cases, the major source of the discrepancy is the increase of the melt density with chain lengths (in the range of small lengths). In the present simulations, the density is independent of  $N$  and the Rouse behavior is observed for sufficiently short chains. For large  $N$ , the chain length dependence of  $D$ , shown in Fig. 2d, is consistent with the theoretical prediction  $D \sim N^{-2.4}$ , assuming a combination of reptation and CLF. Pure reptation would lead to the scaling relation  $D \sim N^{-2}$ . Taking also CLF into account, one expects a relation close to  $D \sim N^{-2.4}$  over a wide range of molecular weights [4]. Similar scaling relations have

also been observed experimentally [66, 67].

## B. Dynamics of the end-to-end vector

The overall relaxation of polymer chains can be investigated by analyzing the dynamics of the end-to-end vector, quantified via the autocorrelation function

$$P(t) = \frac{\langle \mathbf{R}(t) \cdot \mathbf{R}(0) \rangle}{\langle \mathbf{R}(0) \cdot \mathbf{R}(0) \rangle}, \quad (5)$$

with  $\mathbf{R}(t)$  being the end-to-end vector at time  $t$  and  $\langle \rangle$  denoting averaging over different chains and time origins in a trajectory. This quantity is related to dielectric relaxation spectroscopy measurements [4, 68]. More specifically, the so-called dynamic susceptibility  $\chi''(\omega) = \omega \int_0^\infty P(t) \cos(\omega t) dt$  is expected to behave very similarly to the dielectric loss function of the type A polymers [41].

The simulation results for  $P(t)$  and  $\chi''(\omega)$  are shown in Fig. 3a,b, and Fig. 3c, respectively. For the calculation of  $\chi''(\omega)$ , we fitted  $P(t)$  with a series of exponential functions (Debye modes),  $P(t) = \sum_i a_i \exp(t/\tau_i)$ , giving  $\chi''(\omega) = \sum_i a_i \omega \tau_i / (1 + \omega^2 \tau_i^2)$ . In Fig. 3b,c, we have rescaled  $t$  and  $\omega$  with the mean relaxation time, defined as  $\tau_{\text{ch}} = \int_0^\infty P(t) dt$ , to make the curves comparable.

The Rouse model and the pure reptation model both predict a similar relation for  $P(t)$  [2]:

$$P_{\text{Rouse/rep}}(t) = \frac{8}{\pi^2} \sum_{p, \text{odd}} \frac{1}{p^2} \exp(-\frac{p^2 t}{\tau_1}), \quad (6)$$

where  $\tau_1$  is the longest relaxation time of the chain, *i.e.*,  $\tau_1 = \tau_R$  in the Rouse model and  $\tau_1 = \tau_d$  in the reptation model. According to this equation, the mean relaxation time should be given by  $\tau_{\text{ch}}^{\text{Rouse/rep}} = (\pi^2/12)\tau_1$ , and all curves for  $P(t)$  should collapse onto a single master curve if plotted against  $t/\tau_{\text{ch}}$ . Furthermore, the quantity  $(1 - P(t))$  should scale as

$$\begin{aligned} 1 - P(t) &= \frac{8}{\pi^2} \sum_{p, \text{odd}} \frac{1}{p^2} (1 - e^{-p^2 t/\tau_1}) \\ &\approx \frac{4}{\pi^2} \int_0^\infty dp \frac{1}{p^2} (1 - e^{-p^2 t/\tau_1}) = \frac{4}{\pi^{3/2}} \left(\frac{t}{\tau_1}\right)^{1/2} \end{aligned} \quad (7)$$

for  $t \ll \tau_1$ , which corresponds to a scaling behavior  $\chi''(\omega) \sim \omega^{-1/2}$  of the dynamic susceptibility at  $\omega \gg \tau_1^{-1}$ .

In order to test these predictions, we first compare the curves for  $P(t)$  vs.  $t/\tau_{\text{ch}}$  in Fig. 3b with the prediction of Eq. (6) (symbols). The curves clearly do not collapse. The simulation data for  $P(t)$  at chain lengths  $N = 50$  and  $N = 100$  are close to the prediction of Eq. (6), however, for shorter chains the  $P(t)$  curves are less stretched than this relation and for longer chains deviations from this relation become gradually more pronounced and the curves for  $P(t)$  become more and more stretched. This behavior is

consistent with the gradual stretching of the dielectric relaxation curves with increasing chain length, as detected experimentally [69]. Furthermore,  $P(t)$  can be written as the sum of the autocorrelations of the odd Rouse modes of the chain [2, 68] and the gradual stretching of  $P(t)$  is consistent with the gradual stretching of the autocorrelation of the Rouse modes with increasing chain length, as observed previously [27, 60].

Fig. 3c shows the corresponding  $\chi''(\omega)$  curves alongside with the prediction of Eq. (6) which predicts a peak at  $\omega \tau_{\text{ch}} \approx 1$  followed by the power law decay mentioned above,  $\chi''(\omega) \sim \omega^{-1/2}$  on the high frequency side. Consistent with the trend observed in Fig. 3b, for short chains, the curves seem close to the theoretical prediction; for large chain lengths  $N$ , however, the peak shifts to smaller  $\omega \tau_{\text{ch}}$ -values and broadens, and the slope of  $\log(\chi''(\omega))$  vs.  $\log \omega$  at high frequencies gradually deviates from  $-1/2$  and approaches  $-1/4$ . These observations are consistent with the results of dielectric relaxation spectroscopy experiments on entangled melts [41–43]. Although, we should note that experiments on highly entangled melts show the appearance of two scaling regimes on the high-frequency side of the relaxation peak:  $\omega^{-1/4}$  scaling at high frequencies (far from the peak frequency) and  $\omega^{-1/2}$  scaling regime at lower frequencies, close to the peak frequency [41–43]. In the range of chain length studied here, we do not still see the  $\omega^{-1/2}$  scaling regime for entangled chains. A qualitatively similar chain-length-dependent shape of the dielectric relaxation curve has also recently been observed in multiscale simulations of polyisoprene melts of different lengths [22].

Finally, Fig. 3d tests the scaling behavior of  $(1 - P(t))$  vs.  $t/\tau_{\text{ch}}$  in a double logarithmic plot, where  $(1 - P(t))$  is scaled with  $(t/\tau_{\text{ch}})^{1/4}$ , again showing the prediction of Eq. (6) for comparison. Whereas the theory curve (symbols) features the expected  $t^{1/2}$  scaling for all times below  $t < \tau_{\text{ch}}$ , none of the simulation curves follows this behavior strictly.  $(1 - P(t))$  has a rich structure and its slope is both time and  $N$  dependent. Particularly, upon increasing chain length, a region corresponding to  $(1 - P(t)) \sim t^{1/4}$  gradually emerges. Such a scaling regime has been previously observed in the slip-spring simulations as a plateau region in the plot of  $-t^{3/4} \partial P / \partial t$  vs.  $t$  [45].

As will be discussed below, the  $\omega^{-1/4}$  and  $t^{1/4}$  behaviors of  $\chi''(\omega)$  and  $(1 - P(t))$ , respectively, can be explained by CLF. This behavior originates from the restricted Rouse motion of the chain inside the tube in the interval of  $\tau_e < t < \tau_R$ , which also leads to the subdiffusive  $t^{1/4}$  scaling of  $g_1(t)$  (regime III of Eq. (3)) [3]. Before discussing this regime in more detail, we analyze the structure of  $P(t)$  by plotting  $(1 - P(t))$  together with  $g_1(t)$ , for  $N = 100, 400$ , and  $1000$ , in Fig. 4. In this figure, both functions are normalized by  $t^{1/2}$ . Furthermore, to facilitate the comparison,  $g_1(t)/t^{1/2}$  is divided by  $R_{\text{ee}}^2$ , such that both functions have similar values at short times.  $(1 - P(t))$  approximately follows the time-dependence of  $g_1(t)$ . At short times, before feeling entanglements ( $t < \tau_e$ ),  $(1 - P(t))$  first scales approximately with  $t$

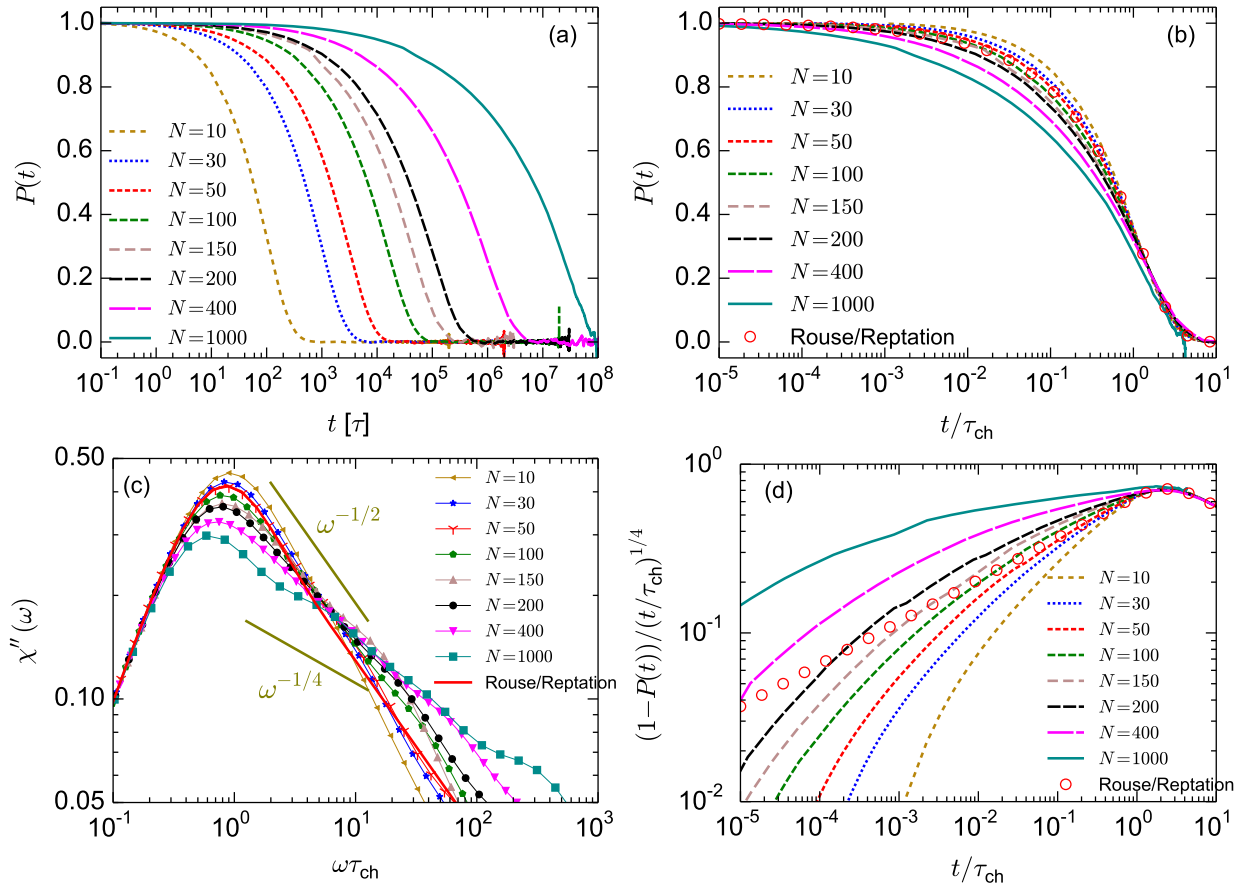


FIG. 3. (a) Autocorrelation function of the end-to-end vector,  $P(t)$  vs. time  $t$ . (b) Same data vs.  $\tau/\tau_{\text{ch}}$ , where  $\tau_{\text{ch}}$  is the mean relaxation time of  $P(t)$ . (c) Same data in the frequency domain. Here the dynamic susceptibility,  $\chi''(\omega)$ , is shown as a function of  $\omega\tau_{\text{ch}}$ . (d)  $(1 - P(t))/(t/\tau_{\text{ch}})^{1/4}$  vs.  $t/\tau_{\text{ch}}$ .

and then with  $t^{1/2}$ ; this latter scaling regime is the one expected for a free Rouse chain (as Eq. (7) shows). After these short-time regimes, the  $(1 - P(t))/t^{1/2}$  of sufficiently long chains (similar to their  $g_1(t)/t^{1/2}$ ) exhibits a negative slope which tends to  $-1/4$  upon increasing  $N$  (*i.e.*,  $(1 - P(t)) \sim t^{1/4}$  corresponding to regime III in Eq. (3)). For  $N = 100$  (and shorter chains), the negative slope of  $(1 - P(t))/t^{1/2}$  before the terminal time is negligible. At late times ( $t > \tau_d$ , when  $g_1(t)$  has normal diffusion)  $P(t)$  tends to zero and  $(1 - P(t))/t^{1/2} \sim 1/t^{1/2}$ . In the range of chain length studied here, corresponding to  $g_1(t) \sim t^{1/2}$  in the interval of  $\tau_R < t < \tau_d$ , a clearly separated regime of  $(1 - P(t)) \sim t^{1/2}$  (in that time range) is not observed. For longer chains, where the decay of  $P(t)$  until  $\tau_R$  becomes small and the separation between  $\tau_R$  and  $\tau_d$  becomes large, it is expected that a regime of  $(1 - P(t)) \sim t^{1/2}$  in the range of  $\tau_R < t < \tau_d$  is observed. Such a regime corresponds to scaling regime  $\chi''(\omega) \sim \omega^{-1/2}$  of the dynamic susceptibility, which has indeed been observed experimentally [41–43] in the range  $\tau_d^{-1} < \omega < \tau_R^{-1}$  as mentioned earlier.

We continue with a discussion of the  $(1 - P(t)) \sim t^{1/4}$  regime in terms of CLF. For this, we make use of a central

quantity of the tube model, the “surviving tube fraction”,  $\mu(t)$ , which is the fraction of the (primitive) chain that is still trapped in the original tube formed at  $t = 0$ . When some parts of the chain escape from the original tube (formed at  $t = 0$ ), they become orientationally decorrelated from the orientation of the chain at  $t = 0$ , and only the orientations of the segments that are still trapped inside the tube remain correlated with that at  $t = 0$ . Therefore, in the absence of CR (because the argument assumes a fixed tube in space),  $P(t)$  is equal to  $\mu(t)$  [2, 4, 41]. Note that this argument ignores the decay of  $P(t)$  due to the very short time Rouse motion of the chain inside the tube, before feeling entanglements ( $t < \tau_e$ ); for long chains, this motion leads to a very small decay of  $P(t)$ . For pure reptation  $\mu(t)$  is expressed by Eq. (6) (*i.e.*, it equals  $P_{\text{rept}}(t)$ ). However, pure reptation does not take into account the restricted Rouse motion of the chain in the tube in the range of  $\tau_e < t < \tau_R$ . The effect of the restricted Rouse motion on  $\mu(t)$  is discussed in terms of CLF in the literature [2, 3, 56]. CLF leads to the escape of a portion of the segments from the tube, which has been quantified via the following simple functional

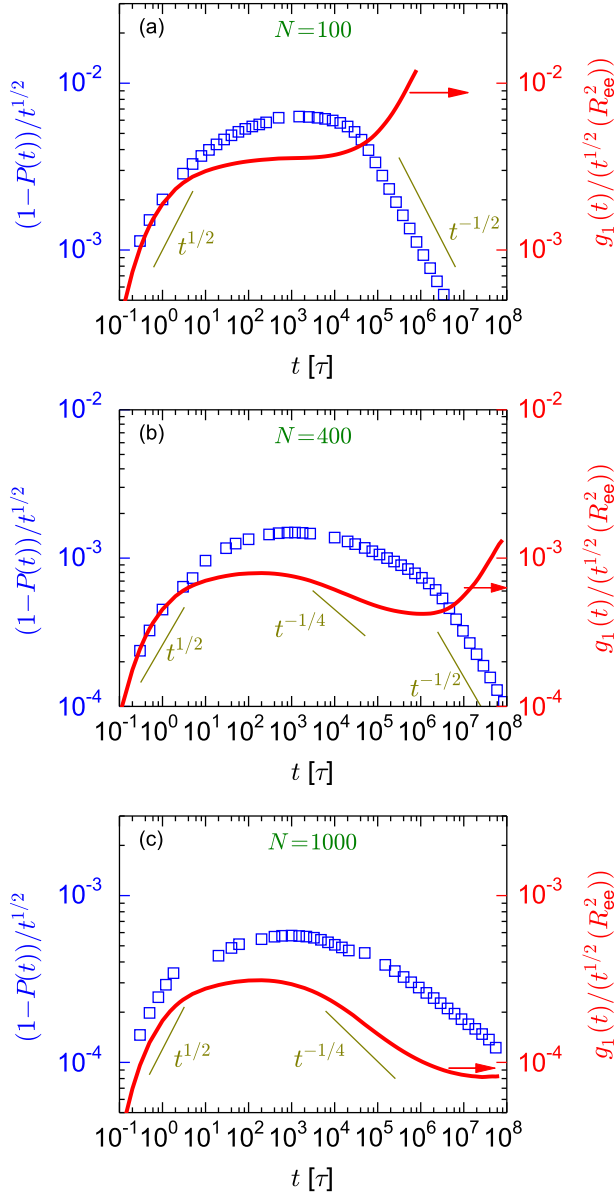


FIG. 4.  $(1 - P(t))/t^{1/2}$  together with rescaled  $g_1(t)/t^{1/2}$  (averaged over all monomers) vs. time  $t$ . Panels (a), (b), and (c) show the curves for  $N = 100$ ,  $N = 400$ , and  $N = 1000$ , respectively.

form [56]:

$$\mu(t) = 1 - \frac{C}{Z} \left(\frac{t}{\tau_e}\right)^{1/4}, \quad t < \tau_R, \quad (8)$$

where  $Z = N/N_e$  and  $C = 1.5$  according to Likhtman and McLeish [56]. The above  $t^{1/4}$  scaling of the escaped segments (*i.e.*,  $1 - \mu(t)$ ) originates from the restricted Rouse motion of the chain [3], which also leads to the  $t^{1/4}$  scaling of  $g_1(t)$ . Considering the equality of  $\mu(t)$  and  $P(t)$  in the absence of CR (for  $t > \tau_e$ ), the emergence of  $(1 - P(t)) \sim t^{1/4}$  for long chains, as suggested by Fig. 3d, is consistent with the above relation. It is also worth men-

tioning a comment about the effect of CR on  $P(t)$ . The end-to-end correlation of chains in monodisperse linear polymer melts is dominated by reptation and CLF, and the effect of CR decreases with increasing chain length. According to the ‘‘Rouse-tube’’ model of CR, the tube behaves as a Rouse chain of  $Z = N/N_e$  segments. The average local relaxation time of each segment is the disentanglement time of a surrounding chain, which scales with  $Z^{3.4}$ , and the overall relaxation time of the tube due to CR events scales with [4]  $Z^2 \cdot Z^{3.4} = Z^{5.4}$ . For large values of  $Z$ , the CR relaxation time of the tube is much longer than the disentanglement time and hence  $P(t)$  of long chains is not expected to be largely affected by the CR process. The effect of CR on the  $P(t)$  of monodisperse linear polymers has also been studied experimentally for  $Z \approx 4$  up to  $Z \approx 35$  by comparing the relaxation of chains in quasi monodisperse melts with that in blends containing very long chains [70]. It has been reported that the CR mechanism accelerates the dielectric relaxation (corresponding to relaxation of the end-to-end vector), however, the effect decreases with increasing  $N$ . Suppression of CR, via blending with very long chains, has been reported to increase the dielectric relaxation time around 35% for  $Z \approx 20$  and around 22% for  $Z \approx 35$  [70]; these values correspond to the relaxation times of around 9% and 6% longer chains. Based on these considerations, we do not consider CR and compare the measured  $P(t)$  curves with the following analytical relation, proposed by Likhtman and McLeish [56], for the evolution of  $\mu(t)$  due to CLF at short times and reptation at later times:

$$\begin{aligned} \mu(t) = & \int_{\varepsilon^*(Z, \tau_e)}^{\infty} \frac{0.306}{Z \tau_e^{1/4} \varepsilon^{5/4}} \exp(\varepsilon t) d\varepsilon \\ & + \frac{8\tilde{G}_f(Z)}{\pi^2} \sum_{p, \text{odd}}^{p^*(Z)} \frac{1}{p^2} \exp\left(-\frac{p^2 t}{\tau_{df}(Z, \tau_e)}\right). \end{aligned} \quad (9)$$

Among others, this equation has been used for describing the experimental dielectric relaxation curves of entangled polymer melts [43, 71]. The first term of Eq. (9) is the contribution of CLF and dominates up to times of the order of  $\tau_R$ . This term is responsible for the scaling  $(1 - \mu(t)) \sim t^{1/4}$  (see Eq. (8)). The second term is the contribution of reptation which dominates at times longer than  $\tau_R$ . For large values of  $Z$ , this term leads to a scaling  $(1 - \mu(t)) \sim t^{1/2}$  up to the terminal time (see also Eq. (7)). The time  $\tau_{df}(Z)$  is the disentanglement time in the presence of CLF, and  $\tilde{G}_f(Z)$  is a dimensionless plateau modulus. Explicit expressions for the relations between these quantities and  $\varepsilon^*$  and  $p^*$  can be found in Likhtman and McLeish [56]. The quantities  $Z = N/N_e$  and  $\tau_e$  are the only input variables in Eq. (9). In our analysis, we set  $N_e = 52$ , which is the value extracted from the plateau modulus (see Section II and Table I) and calculate  $\tau_e$  from  $\tau_e = \tau_0 N_e^2 = 1.47 N_e^2$  (see Section III A).

Fig. 5 compares the simulation data (symbols) for  $P(t)$  with the results of Eq. (9) (solid lines) for chain lengths  $N = 200$ ,  $N = 400$ , and  $N = 1000$  in two different presentations. For  $N = 200$ , Eq. (9) does not satisfactorily



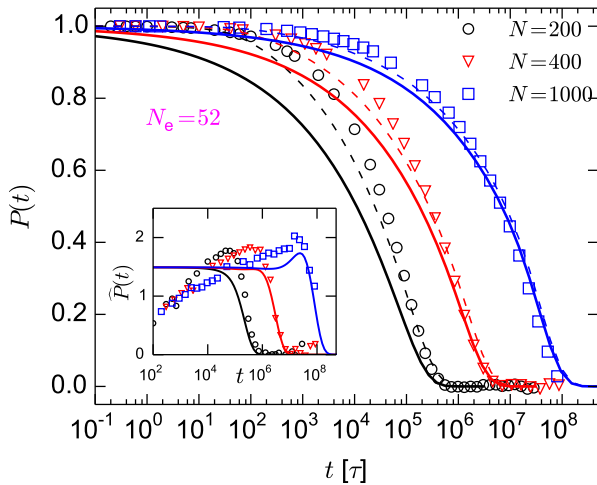


FIG. 5. (a) The  $P(t)$  data for  $N = 200, 400,$  and  $1000$  (symbols) compared with the prediction for  $\mu(t)$  of the Likhtman-McLeish model, Eq. (9). The solid lines are the results of the original model (Eq. (9)) using  $N_e = 52$  (estimated from the plateau modulus). The dashed lines show the results of the modification proposed by Hou *et al.* [37] where the upper bound of the integration in Eq. (9) is replaced by  $(\alpha^4 \tau_e)^{-1}$ .  $\alpha = 0.35$  is used here. Inset: same data in the presentation adopted by Likhtman and McLeish [56]; here  $\hat{P}(t) = -4Z\tau_e^{1/4}t^{3/4}\partial P/\partial t$ .

describe  $P(t)$ . This is to be expected, since Eq. (9) predicts an initial scaling regime  $(1 - P(t)) \sim t^{1/4}$ , which is not yet developed for such mildly entangled chains. However, the quality of fitting increases with increasing  $N$ , and for  $N = 1000$ , a fair agreement between the measured  $P(t)$  and Eq. (9) is obtained, if one excludes the early regimes I and II of unrestricted Rouse motion, which do not contribute significantly to the decay of  $P(t)$ . To show the effect of  $N_e$  on the prediction of the model (Eq. (9)), in SI, Figure S2, the results of using  $N_{e,\text{ppa}} = 87$  obtained from the primitive path analysis, are shown. With  $N_{e,\text{ppa}} = 87$ , the deviation between the model and the simulation data is large, as compared to the results of using  $N_e = 52$ .

In their study of the viscoelastic properties of polymer melts, Hou *et al.* [37] suggested replacing the upper bound of integration in the first term of Eq. (9) by  $(\alpha^4 \tau_e)^{-1}$ , where  $\alpha$  is a fitting parameter, and rescaling  $\mu(t)$  such that it starts from 1 at  $t = 0$ . This eliminates the main contribution to the decay of  $\mu(t)$  at times shorter than around  $(\alpha^4 \tau_e)$ . Here, we also show the results of this modified equation in Fig. 5 (dashed lines;  $\alpha = 0.35$ ). The behavior for short chains improves albeit at the expense of introducing a fitting parameter. The output is sensitive to the value of  $\alpha$  as the bound of integration changes with  $\alpha^4$ .

We close this section by discussing the average and the longest relaxation times of  $P(t)$ ,  $\tau_{\text{ch}}$  and  $\tau_1$ , respectively. They are shown in Fig. 6. The relaxation times are divided by  $N^2$ . The time  $\tau_1$  has been estimated from

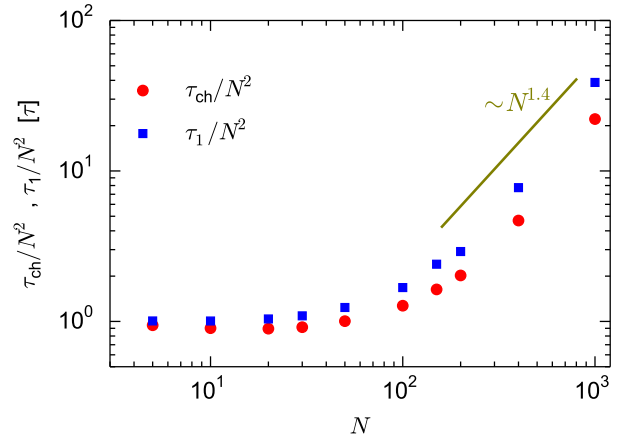


FIG. 6. Average relaxation time  $\tau_{\text{ch}} = \int_0^\infty P(t)dt$  and maximum relaxation time  $\tau_1$  of  $P(t)$  vs. chain length  $N$ .

the relaxation time of the slowest exponential mode used for the fitting of  $P(t)$ . In the range of chain lengths  $N$  studied here,  $\tau_1/\tau_{\text{ch}}$  increases with increasing  $N$ , due to the fact that the  $P(t)$  curves are gradually more stretched. The  $N$  dependence of  $\tau_1$  shows a gradual change from the Rouse behavior ( $\tau_1 \sim N^2$ ) to entangled behavior. As mentioned above, based on the reptation and CLF mechanisms, we expect  $\tau_1 \sim N^\alpha$  with  $\alpha \approx 3.4$  over a wide range of molecular weights [4, 6]. This is consistent with the behavior observed here. Similar scaling behavior was previously observed for polyisoprene melts via multiscale simulations [22] and also dielectric relaxation spectroscopy experiments [70, 72].

### C. Single-chain dynamic structure factor

In this section, we discuss the dynamic structure factor of single chains, which characterizes the dynamics of the chain at different length scales and time scales. It is defined as

$$S(q, t) = \frac{1}{N} \sum_{m,n}^N \langle \exp\{i\mathbf{q} \cdot [\mathbf{r}_m(t) - \mathbf{r}_n(0)]\} \rangle, \quad (10)$$

where the sum is taken over the monomers of a chain. Fig. 7a shows the chain length dependence of  $S(q, t)/S(q, 0)$  at  $q = 2.0\sigma^{-1}$ . This  $q$  value corresponds to the length scales much smaller than the tube diameter ( $2\pi/a = 0.66 \sigma^{-1}$ ) and also smaller than, although comparable to, the size of the smallest studied chain ( $2\pi/R_{ee}^{N=10} \approx 1.75 \sigma^{-1}$ ). Based on the Rouse model,  $S(q, t)/S(q, 0)$  is independent of the chain length on length scales smaller than the chain size,  $q \gg 2\pi/R_{ee}$ [2]. Also, entangled chains are expected to behave similarly at length scales much smaller than tube diameter ( $q \gg 2\pi/a$ ) where the chains do not yet feel the entanglement constraints. The results shown in Fig. 7a are consistent

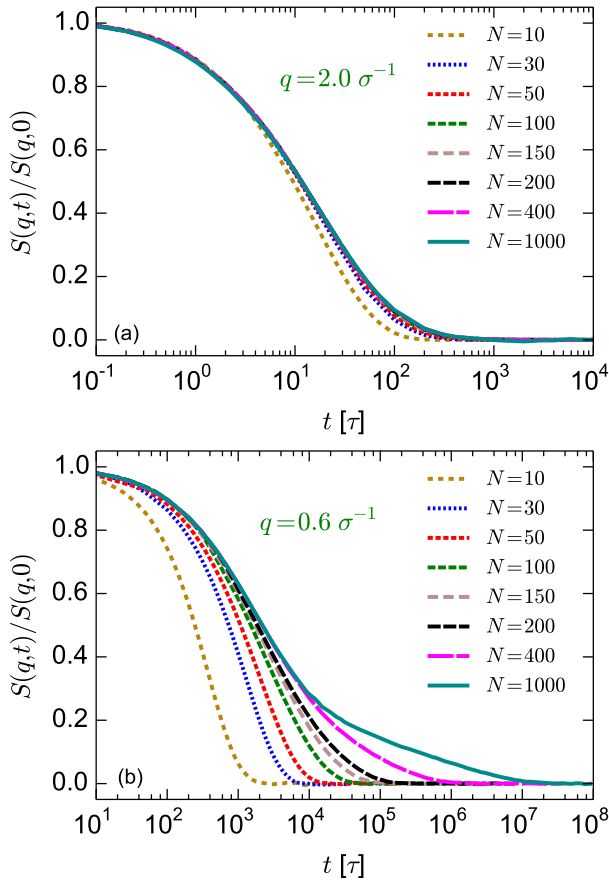


FIG. 7. (a) Normalized dynamic structure factor  $S(q,t)/S(q,0)$  vs. time  $t$  (a) at  $q = 2\sigma^{-1}$ , corresponding to a length scale much smaller than the tube diameter, and (b)  $q = 0.6\sigma^{-1}$  corresponding to a length scale comparable to the tube diameter ( $2\pi/a = 0.66\sigma^{-1}$ ).

with this theoretical expectation and at  $q = 2.0\sigma^{-1}$ ,  $S(q,t)/S(q,0)$  for all studied chains are similar.

Fig. 7b shows the  $S(q,t)/S(q,0)$  at  $q = 0.6\sigma^{-1}$ . This  $q$  value corresponds to a length scale comparable to the tube diameter, however larger than the end-to-end distances of the chains with length  $N < 50$ . At length scales larger than the chain size ( $q \ll 2\pi/R_{ee}$ ),  $S(q,t)$  is controlled by the self-diffusion coefficient of the chains,  $S(q,t)/S(q,0) = \exp(-Dq^2t)$ ; this explains the chain-length dependence of  $S(q,t)/S(q,0)$  at  $q = 0.6\sigma^{-1}$  for  $N \leq 50$ . For  $N \geq 100$ , the short-time behavior of  $S(q,t)$  is almost chain length independent, but, at long times  $S(q,t)$  develops a pronounced  $N$ -dependent shoulder. Previously, Hsu and Kremer [27] studied the chain length dependence of  $S(q,t)/S(q,0)$  for long entangled chains and they also observed similar behavior. Qualitatively similar behavior has also been observed in neutron spin echo experiments [31]. According to the tube model,  $S(q,t)$  of entangled polymers, in length scales larger than the tube diameter and smaller than the chain size, has a two-step decay: the first step originates from the local motion of the chain inside the tube, and the second

step comes from the escape of the chain from the tube (creep) [32]. The characteristic time of the local process is chain length independent whereas that of the creep process is disentanglement time,  $\tau_d$ , which strongly scales with  $N$  ( $\sim N^{3.4}$ ) [32]. The trend observed in Fig. 7b is in qualitative agreement with the expected behavior of  $S(q,t)$  based on the tube model.

Fig. 8a-b shows the  $q$ -dependence of  $S(q,t)/S(q,0)$  for  $N = 400$  and  $N = 1000$ . This figure covers the range from  $q = 2\pi/R_{ee}$  to  $q = 0.8\sigma^{-1}$ . The latter  $q$  value corresponds to a length scale rather smaller than the tube diameter ( $2\pi/a = 0.66\sigma^{-1}$ ), and even at this length scale,  $S(q,t)$  exhibits a shoulder. With decreasing  $q$ , the height of the shoulder increases. As mentioned above, based on the tube model, in the range of  $2\pi/R_{ee} \ll q \ll 2\pi/a$  the long-time behavior (*i.e.*, the shoulder) of  $S(q,t)$  is governed by the creep process which has a  $q$ -independent characteristic time of  $\tau_d$  (in the absence of CR) [2, 32]. This expectation is based on the following argument [2, 32]:  $S(q,t)$  is dominated by the pair of monomers for which  $|\mathbf{r}_m(t) - \mathbf{r}_n(0)| < 2\pi q^{-1}$ . At time  $t$ , a monomer that has escaped from the tube is separated from monomers inside the original tube (formed at time 0) by distances comparable to the chain size. Thus, for  $q$  values corresponding to length scales much smaller than the chain size, pairs containing an escaped particle do not contribute to  $S(q,t)$ , and the long-time behavior of  $S(q,t)$  should be controlled by (and be proportional to) the fraction of monomers which are still confined in the original tube, *i.e.*, the surviving tube fraction,  $\mu(t)$ . This argument assumes that the tube is fixed in space and therefore neglects CR. In the absence of CR, we have  $\mu(t) = P(t)$  and the argument thus predicts  $S(q,t)/S(q,0) \propto P(t)$  at late times. The proportionality constant, which is the amplitude of the creep process is predicted to be  $\exp(-q^2a^2/36)$  [4, 28, 32]. Therefore, the tube model, in the absence of CR, predicts that in the range of  $2\pi/R_{ee} \ll q \ll 2\pi/a$  the long-time behavior of  $S(q,t)$  can be described by  $S(q,t)/S(q,0) = \exp(-q^2a^2/36) P(t)$ . Therefore, it is also expected that in that  $q$  range, the shoulder of  $S(q,t)/S(q,0)$  has a  $q$ -independent characteristic (decay) time. We do not observe this for the chain lengths studied here, and the times where  $S(q,t)/S(q,0)$  vanishes in Fig. 8 do not coincide over a  $q$  range. More explicitly, the proportionality of  $S(q,t)$  and  $P(t)$  is not observed. Fig. 8c shows  $S(q,t)$  at  $q = 0.4\sigma^{-1}$  and  $q = 0.5\sigma^{-1}$  together with the corresponding  $\exp(-q^2a^2/36) P(t)$  curves for  $N = 1000$ . One can see that the long-time decay of  $S(q,t)/S(q,0)$  is significantly faster than that of  $P(t)$ . This signals the importance of CR in the relaxation of  $S(q,t)$ , at least for the chain lengths studied here. We note that, to our knowledge, the long-time regimes of  $S(q,t)$  and  $P(t)$  have not been compared experimentally, most probably because of the limited time window of neutron spin echo experiments.

The argument sketched above for discussing the long-time behavior of  $S(q,t)$ , relies on the assumption that there are two classes of monomers: Monomers that are still trapped inside the tube after a time  $t$  whose displace-

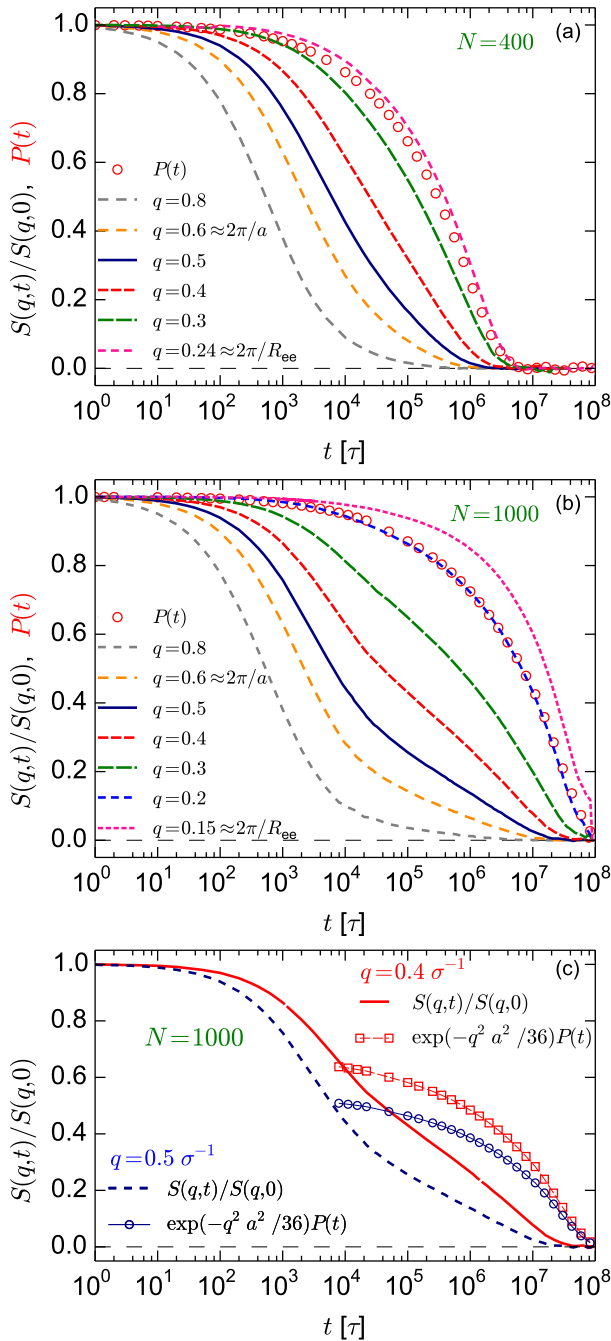


FIG. 8. (a,b) Normalized dynamic structure factor  $S(q,t)/S(q,0)$  vs. time  $t$  for different  $q$ -vectors at chain length  $N = 400$  (a) and  $N = 1000$  (b). Also shown for comparison is  $P(t)$ , the autocorrelation function of the end-to-end vector. (c)  $S(q,t)/S(q,0)$  of  $N = 1000$  at  $q = 0.4\sigma^{-1}$  and  $q = 0.5\sigma^{-1}$  together with the corresponding  $\exp(-q^2 a^2 / 36)P(t)$  functions.

ments are restricted, and monomers that have escaped from the tube and have larger displacements. This heterogeneity can be visualized by calculating the second-order non-Gaussian parameter  $\alpha_2(t) = 3\langle\Delta r^4\rangle/5\langle\Delta r^2\rangle^2 - 1$ , where,  $\langle\Delta r^2\rangle = g_1(t)$  is the mean-squared displacement of the monomers. Fig. 9 shows the  $N$  dependence of  $\alpha_2(t)$ .

At short times,  $\alpha_2(t)$  exhibits a very small  $N$ -independent peak, originating from the interparticle caging effect. At later times,  $\alpha_2(t)$  features a second peak which becomes higher with increasing  $N$ . This behavior has been observed previously for different model chains [73, 74]. For comparison, we have also calculated  $\alpha_2(t)$  for the ideal Rouse chains with lengths  $N = 100$  and  $N = 1000$ , through Brownian dynamics simulations of ensembles of non-interacting Gaussian chains (data not shown). The resulting curves are almost chain-length independent when plotted against  $t/\tau_R$ ; they also feature a peak, which can be attributed to the motion of the end monomers, but the maximum is around 0.05 (almost equal to the maximum of  $\alpha_2(t)$  for  $N = 30$  in Fig. 9). In contrast, the peak values of  $\alpha_2(t)$  in the model bead-spring chains are much larger and increase with increasing chain length. This supports the picture discussed above regarding the existence of two groups of monomers with small and large displacements for long chains. However, for the studied chain lengths, the heterogeneity of displacements is not still large enough to see the proportionality of  $S(q,t)/S(q,0)$  and  $P(t)$ . Note that, similar to the Rouse chains, the monomers with large displacements are the monomers near the chain ends because the end monomers escape the tube before the central monomers. However, as discussed above, the intra-chain dynamical heterogeneity of entangled chains is qualitatively different from the corresponding property of the Rouse chains. The inset of Fig. 9 shows  $\alpha_2(t)$  together with  $P(t)$  for  $N = 1000$ . The development of the peak of  $\alpha_2(t)$  coincides with the decay of  $P(t)$  and  $\alpha_2(t)$  reaches its maximum before the final decay of  $P(t)$ .

We proceed with a more quantitative comparison of the simulation results with predictions of the tube model. Accounting for the processes of the local motion of the chain inside the tube (local reptation) and the escape

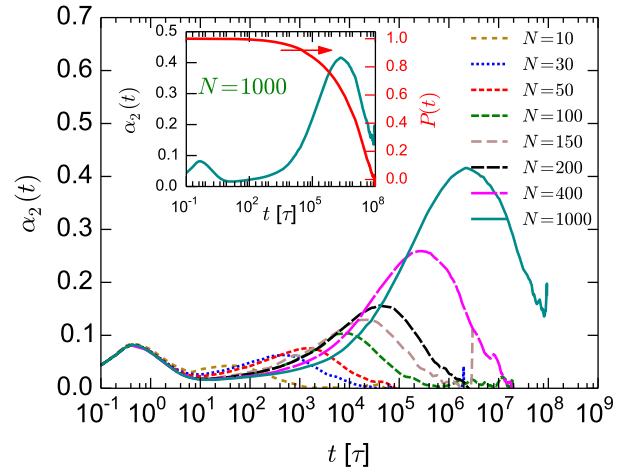


FIG. 9. Non-Gaussian parameter for the displacement of the beads,  $\alpha_2(t)$ , versus time for different chain lengths  $N$  as indicated. Inset:  $\alpha_2(t)$  of  $N = 1000$  together with its  $P(t)$ , the autocorrelation function of the end-to-end vector.

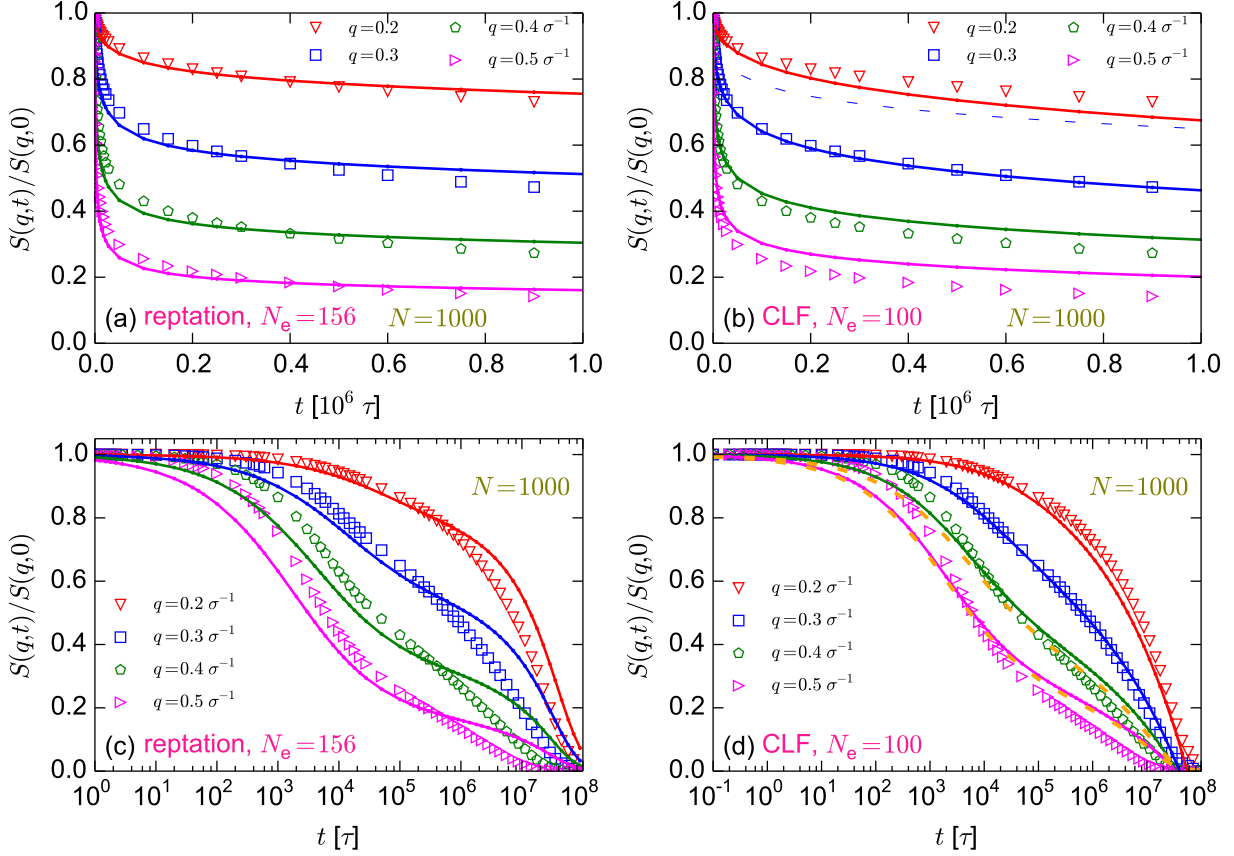


FIG. 10. Simulation results for  $S(q, t)/S(q, 0)$  of  $N = 1000$  for different values of  $q$  (symbols) together with theoretical predictions (solid lines): panels (a) and (c) show, in linear and semi-logarithmic scales, the predictions for  $S(q, t)/S(q, 0)$  based on the pure reptation model (Eq. (11) and Eq. (13)) with  $N_e = 156$  corresponding to  $a = 16.5\sigma$ . Panels (b) and (d) show the predictions based on the CLF model (Eq. (11) and Eq. (14)) with  $N_e = 100$  corresponding to  $a = 13.3\sigma$ . The thin dashed line in (b) shows the result obtained with  $N_e = 52$  (see Table I) at  $q = 0.3 \sigma^{-1}$  for comparison. Yellow dashed lines in (d) show the results obtained with Eq. (15).

of the chain from the tube, the following expression has been proposed for  $S(q, t)$  [4, 28, 32]:

$$\frac{S(q, t)}{S(q, 0)} = [1 - \exp(-\frac{q^2 a^2}{36})] S^{\text{loc}}(q, t) + \exp(-\frac{q^2 a^2}{36}) S^{\text{esc}}(q, t). \quad (11)$$

The first term describes local motion and is calculated using

$$S^{\text{loc}}(q, t) = \exp(\frac{t}{t_{\text{loc}}}) \text{erfc}(\sqrt{\frac{t}{t_{\text{loc}}}}), \quad (12)$$

where  $t_{\text{loc}} = 12\zeta/(k_B T b^2 q^4)$  is the characteristic time of the local process, which is chain length independent and scales with  $q^{-4}$  (it has Rouse behavior). The second term,  $S^{\text{esc}}(q, t)$ , accounts for the escape of the chain from the tube. The following expression has been calculated by assuming the pure reptation process as the only escape

mechanism of the chain [2]:

$$S^{\text{esc}}(q, t) = \frac{1}{S(q, 0)} \sum_{p=1}^{\infty} \left[ \frac{2\nu N}{\alpha_p^2 (\nu^2 + \alpha_p^2 + \nu)} \times \sin^2 \alpha_p \exp(-\frac{4t\alpha_p^2}{\pi^2 \tau_d}) \right], \quad (13)$$

where  $\nu = q^2 N b^2 / 12$  and  $\alpha_p$  are the solutions of  $\alpha_p \tan \alpha_p = \nu$ , and  $\tau_d = \zeta N^3 b^2 / (k_B T \pi^2 N_e)$  is the disentanglement time. Since pure reptation does not provide a proper description of the escaping process (as discussed in section Section III B), the following relation has been calculated for  $S^{\text{esc}}(q, t)$  at  $t < \tau_R$  due to CLF (assuming that CLF dominates escaping process at this time range) [75]:

$$S^{\text{esc}}(q, t) = \frac{1}{S(q, 0)} \frac{N}{2\nu^2} [2\nu + e^{-2\nu} + 2 - 4\nu s(t) - 4e^{-2\nu s(t)} + e^{-4\nu s(t)}]. \quad (14)$$

Here  $s(t) = \psi(t)/2$  and  $\psi(t) = 1 - \mu(t) = 1.5(t/\tau_e)^{1/4}/Z$  is the fraction of segments that has escaped from the

tube due to CLF. At  $t < \tau_R$ , the surviving tube fraction  $\mu(t) = 1 - \psi(t)$  which is identical to Eq. (8).

For comparing the above analytical expressions with the simulation results, we treat  $N_e$  as the only fitting parameter. Eq. (11) has  $a$  as an explicit input; for a given  $N_e$ , we calculate  $a$  using  $a^2 = N_e b^2$ . The expression for  $S^{\text{esc}}(q, t)$  due to CLF (Eq. (14)) has  $N_e$  and  $\tau_e$  as explicit inputs. We calculate  $\tau_e$  for a given  $N_e$  using  $\tau_e = \tau_0 N_e^2$ . Fig. 10 shows the measured  $S(q, t)$  for  $N = 1000$ , together with the theoretical fits in linear and logarithmic presentations. On the linear scale, they are shown up to times of the order of (but smaller than) the Rouse time of chains. Panels (a) and (c) show the results of the pure reptation model. The fit gives the value  $N_e = 156$  for the entanglement length (corresponding to  $a = 16.5 \sigma$ ), which is much larger than  $N_e = 52$  calculated from the plateau modulus. The origin of this discrepancy is the shortcoming of the pure reptation process for the description of the creep process. Here, the ignorance of additional relaxation mechanisms is reflected in much larger apparent tube diameters than expected. Such behavior has also been experimentally observed [75].

Panels (b) and (d) of Fig. 10 present the results of the CLF model, fitted on the simulation data with  $N_e = 100$  (corresponding to  $a = 13.3 \sigma$ ). Eq. (14) is valid for  $t < \tau_R$ , however, in panel (d) it is plotted up to the terminal time, although for fitting only the interval  $t < \tau_R$  is considered. The linear presentation, where the times on the order of  $10^6 \tau$  can be easily seen, might give the impression that the pure reptation model better fits the simulation results than the CLF model; however, the logarithmic presentation reveals that this is not the case. The CLF model fits the  $S(q, t)$  of  $N = 1000$  better than the reptation model, even after  $\tau_R$ ; however, the applicability of Eq. (14) for  $t > \tau_R$  should not be generalized. As illustrated in Fig. 3d, in the case of 1000-bead chains, the slope of  $(1 - P(t))$  vs.  $t$  stays close 1/4 (*i.e.*, the prediction of CLF) up to the terminal time (this would not be the case for longer chains at  $t > \tau_R$ ). The value of  $N_e = 100$  used for fitting the CLF model on the simulation results is significantly smaller than the value calculated from the pure reptation model. This shows the importance of CLF in the process of escaping from the tube (creep process). However,  $N_e = 100$  is still considerably larger than  $N_e = 52$  of the plateau modulus. This is consistent with Fig. 8c which shows a discrepancy between the long-time behaviors of  $P(t)$  and  $S(q, t)$ . As shown in Fig. 5, the  $P(t)$  of chain with length  $N = 1000$  can be fairly described by assuming  $N_e = 52$ ; since  $S(q, t)$  decays significantly faster than  $P(t)$ , a larger apparent entanglement length is needed for the description of  $S(q, t)$  based on the CLF model. This signals the importance of the CR mechanism, which is ignored in the CLF model, for the relaxation of the  $S(q, t)$  of  $N = 1000$ . To assess the sensitivity of the analytical relation to  $N_e$ , Fig. 10b also shows the result for  $S(q, t)$  obtained with  $N_e = 52$  at  $q = 0.3 \sigma^{-1}$  (thin dashed line); it significantly deviates from the simulation data. The  $S(q, t)$  spectra of  $N = 400$  are also compared

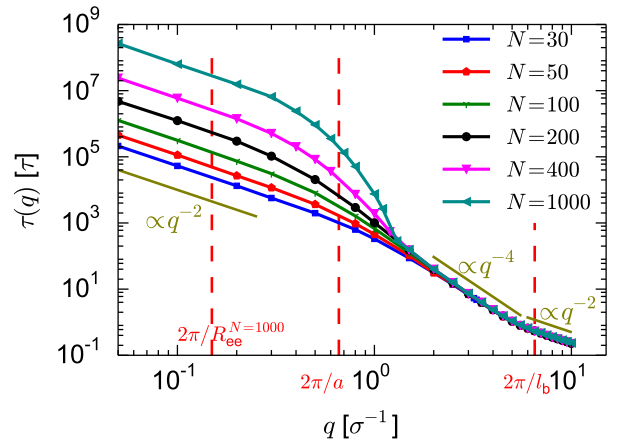


FIG. 11. Effective relaxation time of  $S(q, t)/S(q, 0)$  as calculated from its integral vs. wave vector  $q$ .

with the theoretical models in Figure S3. Like the results of  $N = 1000$ , the CLF model fits the simulation data better than the reptation model. The values of  $N_e$  used for fitting the pure reptation and CLF models to  $S(q, t)$  for  $N = 400$  are close (have around 10% difference) to the ones used in the case of  $N = 1000$ .

Generally, for  $q \gg 2\pi/R_{ee}$ ,  $S^{\text{esc}}(q, t)$  can be approximated by the surviving tube fraction  $\mu(t)$  [2, 32], as explained earlier using a simple argument in the context of Fig. 8. Consistent with this expectation, in the range of  $q \gg 2\pi/R_{ee}$ ,  $S^{\text{esc}}(q, t)$  of the reptation model (Eq. (13)) can be approximated with  $S^{\text{esc}}(q, t) = \mu_{\text{rep}}(t) = P_{\text{rept}}(t)$  which is calculated using Eq. (6) [2, 28]. Also, in this  $q$  range,  $S^{\text{esc}}(q, t)$  of the CLF model (Eq. (14)) reduces to  $S^{\text{esc}}(q, t) \approx \mu(t) = 1 - \psi(t)$  for  $t < \tau_R$  (to see this relation, consider that in  $q \gg 2\pi/R_{ee}$  range,  $\nu$  is large and  $S(q, 0) \approx N/\nu$ ). The above relation can be generalized to times larger than  $\tau_R$ , up to the terminal time, using

$$S^{\text{esc}}(q, t) = \mu^{\text{LM}}(t), \quad q \gg 2\pi/R_{ee}, \quad (15)$$

where  $\mu^{\text{LM}}(t)$  is taken from the Likhman-McLeish model (Eq. (9)) which considers CLF (same as  $\mu(t) = 1 - \psi(t)$ ) and also the long-time reptation process. The dashed yellow lines in Fig. 10d show the results of Eq. (15) for sufficiently large  $q > 2\pi/R_{ee}$ ; for  $N = 1000$ , they are almost identical to the results of the Eq. (14). However, we again note that in general, Eq. (14) is applicable up to  $t < \tau_R$ , while Eq. (15) is valid up to the terminal time.

After the comparison of  $S(q, t)$  with theoretical predictions of the tube model, we will now consider two quantities of special interest that can be derived from  $S(q, t)$ : The spectrum of effective relaxation times  $\tau(q)$  and the closely related wave-vector dependent mobility function  $\Lambda(q)$ .

We define the effective relaxation time  $\tau(q)$  in analogy to  $\tau_{\text{ch}}$  (see Fig. 6), via the integral [76]  $\tau(q) = \int_0^\infty S(q, t)/S(q, 0) dt$ . Fig. 11 shows  $\tau(q)$  vs.  $q$  for different chain lengths. On the smallest scale, where length scales are smaller than the bond length ( $q > 2\pi/l_b$ ),

the beads do not feel the connectivity to other beads; in this regime,  $\tau(q) \sim q^{-2}$  corresponding to the scaling behavior of normal diffusion. This length scale regime corresponds to the time scale regime I of Eq. (3). In the range  $2\pi/a \ll q \ll 2\pi/l_b$ , the beads feel the connectivity along the chain, however, they still do not experience entanglement constraints (corresponding to regime II of Eq. (3)). In this  $q$  range,  $\tau(q) \sim q^{-4}$  which is the scaling behavior of the Rouse chains on scales smaller than the chain size[2]. On length scales that are much smaller than the tube diameter ( $q \gg 2\pi/a$ ),  $\tau(q)$  is almost chain length independent. Upon decreasing  $q$  and approaching length scales comparable to  $a$  (but still smaller than  $a$ ), the values of  $\tau(q)$  for entangled chains increase rapidly and become chain length dependent. As shown in Fig. 7b, this behavior originates from the gradual development of chain-length-dependent shoulders in  $S(q, t)$  of entangled chains. After the step increase of  $\tau(q)$  around  $a$ , the slope of  $\log(\tau(q))$  vs.  $\log(q)$  decreases significantly in the range  $2\pi/R_{ee} < q < 2\pi/a$ . On these length scales, the decay of  $S(q, t)$  results from two relaxation processes with two relaxation times as discussed above, and  $\tau(q)$  results from the contributions of both, but it is dominated by the slow creep process. Finally, on scales  $q < 2\pi/R_{ee}$ , the chains show diffusive behavior with  $\tau(q) \sim q^{-2}$ .

The non-local mobility function  $\Lambda(q)$  is used in dynamical density functional theory calculations of the kinetics of the concentration fluctuations in heterogeneous polymer melts. In fact, the first attempts to analyze  $S(q, t)$  theoretically for entangled polymer melts were motivated by the wish to calculate such non-local mobility functions [77, 78]. The dynamics of concentration fluctuations in a heterogeneous melt, *e.g.*, a blend, is usually described using the following generalized diffusion equation [77, 79]:

$$\begin{aligned} \frac{\partial \phi(\mathbf{r})}{\partial t} &= -\text{div} \mathbf{J} \\ \mathbf{J}(\mathbf{r}) &= - \int d\mathbf{r}' \Lambda(\mathbf{r}, \mathbf{r}') \nabla \mu(\mathbf{r}') , \end{aligned} \quad (16)$$

where  $\Lambda(\mathbf{r}, \mathbf{r}')$  is a non-local mobility coefficient that connects flux at point  $\mathbf{r}$  to the driving force at point  $\mathbf{r}'$ . If the system is translationally invariant with  $\Lambda(\mathbf{r}, \mathbf{r}') = \Lambda(\mathbf{r} - \mathbf{r}')$ , this equation translates to  $J(q) = -\Lambda(q)iq\mu(q)$  in Fourier representation. We have recently proposed to calculate  $\Lambda(q)$  via  $\Lambda(q) = S(q, 0)/(k_B T q^2 N \tau(q))$ , where  $S(q, 0)$  is the single chain form factor and  $\tau(q)$  is the relaxation time of  $S(q, t)/S(q, 0)$  defined above [76].

Fig. 12a shows  $S(q)$  ( $= S(q, 0)$ ), the single-chain form factor (or single-chain structure factor), for chains of different lengths. Also shown for comparison is the form factor of a Gaussian chain of length  $N = 1000$  (symbols), which is given by the Debye function [2],  $S(q)/N = 2/x^2(\exp(-x) + x - 1)$  with  $x = (qR_g)^2$ . The Debye function cannot describe the behavior of the measured  $S(q)$  on small length scales, where the local chain structure is important, but it approximately describes its behavior at length scales larger than the Kuhn length,  $l_k \approx 1.81 \sigma$ . However, a closer look reveals detectable

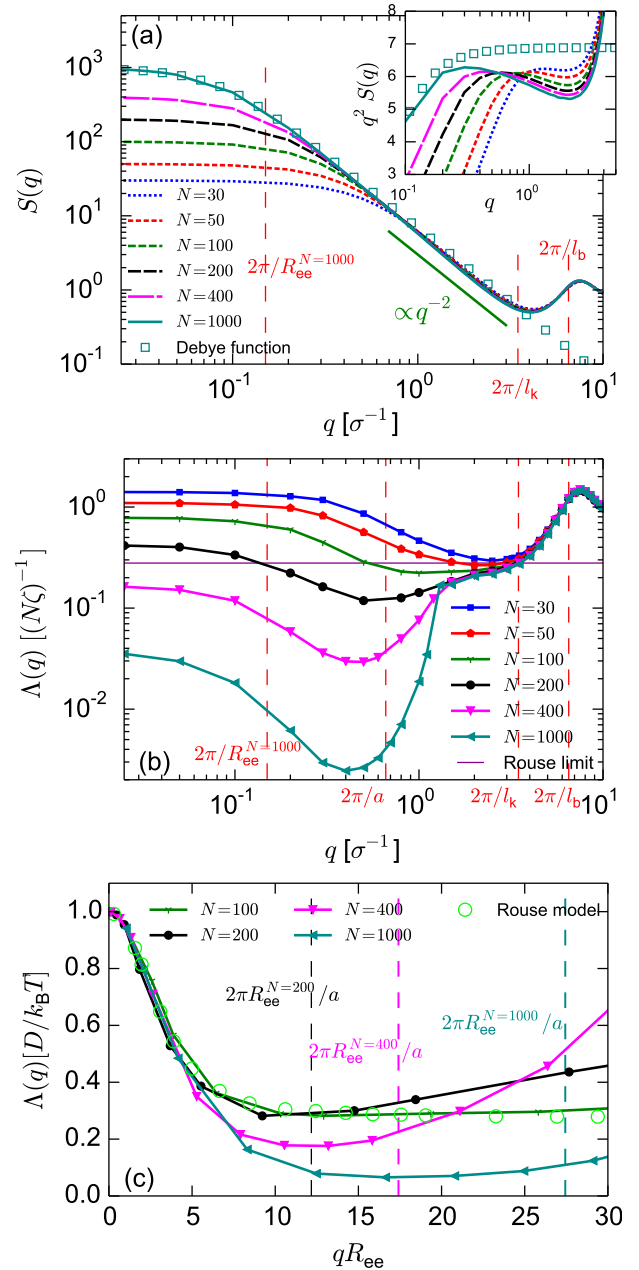


FIG. 12. (a) Single-chain form factor,  $S(q) = S(q, 0)$ , for chains of different lengths. The Debye function, corresponding to the  $S(q)$  of a Gaussian chain, is also shown for  $N = 1000$ . (b) Non-local mobility function,  $\Lambda(q)$ , in units of  $[(N\zeta)^{-1}]$  for chains of different lengths. (c) Non-local mobility function,  $\Lambda(q)$ , in units of  $[D/k_B T]$  vs.  $qR_{ee}$ . The symbols show  $\Lambda(q)$  as calculated from the Rouse model [80] for comparison.

deviations between  $S(q)$  and the Debye function even at length scales larger than  $l_k$ , for all  $N$ . They can be seen in the inset of Fig. 12a which shows  $q^2 S(q)$  vs.  $q$  (Kratky plot); in this presentation, the Debye function exhibits a plateau, which is not seen in the simulation data. Such deviations have been previously observed for different polymer models [18, 22, 81] and have been at-

tributed to the interplay of the chain connectivity and incompressibility of the melt [81].

Fig. 12b shows  $\Lambda(q)$  in units of  $[(N\zeta)^{-1}]$ , where  $\zeta = 25\tau^{-1}$  is the monomeric friction coefficient as determined for long chains, see Section II. In these units, the curves for  $\Lambda(q)$  coincide for all chain lengths at large wavevectors  $q$ . The behavior of  $\Lambda(q)$  reflects the trends observed in Fig. 11 for  $\tau(q)$ . For Rouse chains,  $\tau(q) \sim q^{-4}$  and  $S(q)/N \sim q^{-2}$  in the range of  $q \gg 2\pi/R_{ee}$ . Accordingly,  $\Lambda(q) = S(q)/(k_B T q^2 N \tau(q))$  is constant in this  $q$  range. Based on the Rouse model, one expects this constant to be given by [80] 0.279, and this is indeed seen in the data in Fig. 12b. Entangled chains ( $N > 100$ ) exhibit Rouse behavior in the range of  $2\pi/a \ll q < 2\pi/l_K$ . Upon decreasing  $q$  and approaching length scales comparable to the tube diameter, entanglement effects lead to a rise of  $\tau(q)$  (see Fig. 11) and, consequently, a decrease of  $\Lambda(q)$  for  $N > 100$ .

The large-wavelength behavior of  $\Lambda(q)$  is best evaluated in a different presentation, which uses chain dimensions and chain diffusion coefficient as natural units. Fig. 12c shows the mobility functions in units of  $[D/(k_B T)]$ , where  $D$  is the diffusion constant of the chain, as a function of  $qR_{ee}$ . The plots are shown in the range  $0 < qR_{ee} < 30$ , which is usually relevant for calculations of concentration fluctuations. For comparison, the prediction of  $\Lambda(q)$  as calculated from the Rouse model [80] is also shown (symbols). The simulation data for  $\Lambda(q)$  at chain length  $N = 100$  are very close to the result for the Rouse model. Ideal Rouse chains have a single length scale ( $R_{ee}$ ) and their  $\Lambda(q)$  is chain length independent when presented as a function of  $qR_{ee}$ . This is not the case for entangled melts in which the tube diameter also plays a role; this difference in behavior becomes apparent for  $qR_{ee} > 2\pi$ . Here,  $\Lambda(q)$  drops to lower values and then rises again. However, in the range of  $q < 2\pi/R_{ee}$ , the chains show normal diffusive behavior and  $S(q, t)/S(q, 0) \approx \exp(-Dq^2 t)$ . In this range the expression for  $\Lambda(q)$  simplifies to  $\Lambda(q)[D/(k_B T)] \approx S(q)/N$  which can be approximated with the chain length independent Debye function (shown in Fig. 12a).

#### D. Linear viscoelastic properties

Finally, we discuss the shear stress relaxation modulus, which is the basic linear viscoelastic property of a polymer melt. It can be calculated from the autocorrelation function of shear stresses at equilibrium:

$$G(t) = \frac{V}{k_B T} \langle \sigma_{\alpha\beta}(t) \sigma_{\alpha\beta}(0) \rangle, \quad \alpha \neq \beta, \quad (17)$$

where  $V$  is volume and  $\sigma_{\alpha\beta}(t)$  ( $\alpha, \beta \in \{x, y, z\}$ ) is a shear component of the instantaneous stress tensor. We have used the multiple-tau correlator algorithm [82] to calculate this correlation function, and to improve the statistics, we have averaged over different orientations of the coordinate system [82].

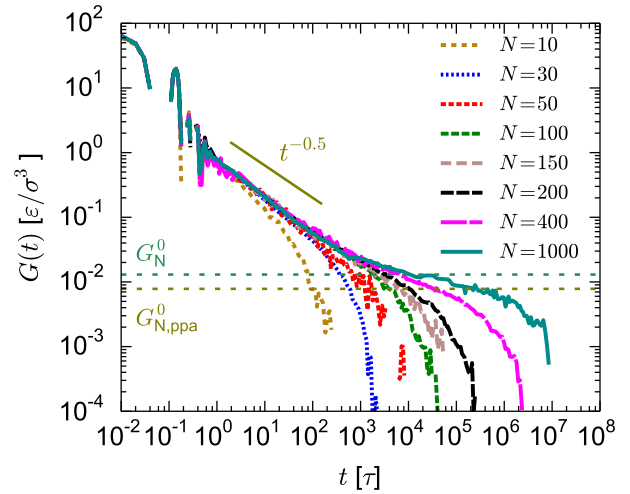


FIG. 13. Shear stress relaxation modulus,  $G(t)$ , vs. time  $t$  for different chain lengths as indicated. The dashed lines mark two values of the plateau modulus,  $G_N^0$ :  $G_N^0 = 0.013\epsilon/\sigma^3$  corresponding to  $N_e = 52$ , which appears to be a reasonable estimate of the plateau modulus, and  $G_{N,ppa}^0 = 0.0078\epsilon/\sigma^3$  corresponding to  $N_{e,ppa} = 87$  (calculated from primitive path analysis) which underestimates the plateau modulus (see text).

The results are shown in Fig. 13. Generally, before the chain relaxation processes, the  $G(t)$  of a polymer melt exhibits the signatures of bond vibrations (appearing as short-time oscillations) and  $\alpha$ -relaxation (appearing as a drop in  $G(t)$  after a glassy plateau at sufficiently low temperatures) [83]. For the current model,  $\alpha$ -relaxation is very fast (it takes place around the short-time peak of the non-Gaussian parameter  $\alpha_2(t)$  in Fig. 9) and it is merged with the bond-vibration process. After these short-time processes, chain relaxation processes take place. The Rouse model predicts  $G(t) \sim t^{-1/2}$  for  $t < \tau_R$ . Entangled chains also exhibit this Rouse scaling before feeling entanglement constraints ( $t < \tau_e$ ). After the  $N$ -independent entanglement time  $\tau_e$ , entangled chains are constrained in their confining tubes and for sufficiently long chains,  $G(t)$  flattens and develops a plateau. Finally, at the disentanglement time  $\tau_d$ , the chains escape from the tubes which leads to the final sharp decay of  $G(t)$ . In the range of chain lengths studied here, the plateau regime is not yet fully developed, but entanglement effect manifests in the emerging  $N$ -dependent shoulders in the  $G(t)$  curves.

The plateau modulus is related to the entanglement length via  $G_N^0 = (4/5)G(\tau_e) = (4/5)\rho k_B T/N_e$ , where  $\rho$  is the number density of monomers. The horizontal dashed lines in Fig. 13 mark two estimates of  $G_N^0$  (see also Section II and Table I): (i)  $G_N^0 = 0.013\epsilon/\sigma^3$  corresponding to  $N_e = 52$ , which was calculated by Likhtman *et al.* for a slip-link model parameterized based on the Kremer-Grest chains [14], and (ii)  $G_{N,ppa}^0 = 0.0078\epsilon/\sigma^3$  calculated from  $N_{e,ppa} = 87$  measured through primitive path analysis [62, 63]. Unfortunately, a direct visual evaluation of the above estimates for  $G_N^0$  based on the simulation data is not

possible, since the curves for  $G(t)$  do not exhibit a well-defined plateau with slope zero. However, we can evaluate the self-consistency of the different estimates by using the relation  $G_N^0 = (4/5)G(\tau_e)$  to extract  $\tau_e$  from the  $G(t)$  curves (for a given  $N_e$ ) in Fig. 13, and comparing this value with that obtained via the relation  $\tau_e = \tau_0 N_e^2$ . The estimate (i),  $G_N^0 = 0.013\varepsilon/\sigma^3$ , yields  $\tau_e \approx 2.9 \cdot 10^3\tau$  for chain length  $N = 400$  and  $\tau_e \approx 4 \cdot 10^3\tau$  for  $N = 1000$ ; these values are very close to the Rouse time  $N_e = 52$  monomers,  $\tau_0 N_e^2 \approx 4 \cdot 10^3\tau$ . However, the estimate (ii),  $G_{N,\text{ppa}}^0 = 0.0078\varepsilon/\sigma^3$  gives  $\tau_e \approx 83 \cdot 10^3\tau$  for  $N = 1000$  and  $\tau_e \approx 15 \cdot 10^3\tau$  for  $N = 400$ ; these values of  $\tau_e$  are strongly  $N$ -dependent and also both are larger than  $\tau_0 N_{e,\text{ppa}}^2 = 11 \cdot 10^3\tau$ . Thus, the estimate  $N_e = 52$  leads to a more consistent overall picture, and  $G_N^0 = 0.013\varepsilon/\sigma^3$  appears to be a reasonable estimate of the plateau modulus. Further discussion of the value of the plateau modulus is provided below. We note that we can also invert this argument and use the self-consistency condition to estimate  $N_e$  and  $G_N^0$  from the simulation data for  $G(t)$ , which would also give  $N_e \approx 52$ . Previously Hsu and Kremer [18] measured the  $G(t)$  of the melts of long semiflexible bead-spring chains; they reported that the entanglement length determined from the primitive path analysis is consistent with the plateau modulus of the measured  $G(t)$  curves. Therefore,  $N_{e,\text{ppa}}$  is not generally inconsistent with the plateau modulus.

In the absence of CR,  $G(t)$  at  $t \gg \tau_e$  is proportional to the surviving tube fraction,  $\mu(t)$  [2, 4]. This means that, stress is sustained by the part of the chain still inside the tube and, in the absence of CR, is only relaxed by escaping from the original tube. In this case, we have  $G(t)/G_N^0 = \mu(t) = P(t)$ . However, for the description of  $G(t)$ , CR effects cannot be ignored. In the Rouse-tube model, CR leads to a Rouse-like motion of the tube and even small-scale Rouse motions of the tube contribute to the relaxation of stress [3, 4]. Combined rheological and dielectric experiments on monodisperse linear polymer melts have suggested the relation [41, 55]  $G(t)/G_N^0 \approx P(t)^{1+\alpha}$  with  $\alpha = 1$ , instead of  $\alpha = 0$  as in the case of ignoring CR. This relation expresses the “double reptation” [84, 85] and “dynamic tube dilation” [41, 55] approximations, which have also been explained based on the Rouse-tube model of CR [4] (a more detailed discussion of the prediction of the Rouse-tube model is also provided below, in the context of Eq. (18)). The proportionality of  $G(t)$  and  $P(t)^2$  has also been observed via the simulation of a slip-link model [47]. Fig. 14 compares  $G(t)$  with  $P(t)$  and  $P(t)^2$  for  $N = 200, 400$ , and 1000. In all cases,  $G_N^0 P(t)^2$  (with  $G_N^0 = 0.013\varepsilon/\sigma^3$ ; solid red lines) describes the late-time behavior of  $G(t)$  reasonably well, and  $G_N^0 P(t)$  (dashed magenta lines), which ignores CR, decays significantly more slowly than  $G(t)$ . The figure also shows that the late time behavior of  $G(t)$  is not captured well if one uses  $G_{N,\text{ppa}}^0$  as prefactor instead of  $G_N^0$ .

We continue the discussion with a comparison of the measured  $G(t)$  data with the Likhtman-McLeish model

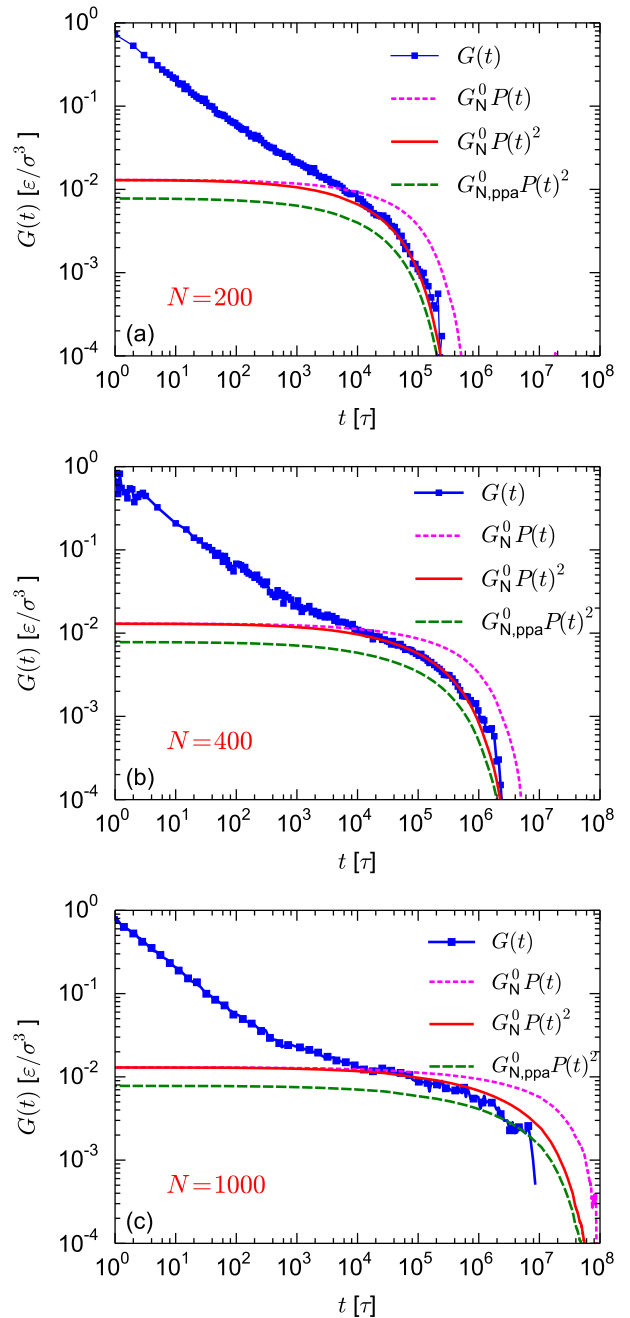


FIG. 14. Simulation data for  $G(t)$  vs.  $t$  (blue) compared to  $G_N^0 P(t)$  (dashed magenta),  $G_N^0 P(t)^2$  (solid red) and  $G_{N,\text{ppa}}^0 P(t)^2$  (dashed green) for chain lengths (a)  $N = 200$ , (b) 400, and (c) 1000.

which accounts for the reptation, CLF, and CR processes, and also the initial short-time Rouse dynamics [56]:

$$\begin{aligned}
 G(t) = & G_e \left[ \frac{1}{Z} \sum_{p=Z}^N \exp\left(-\frac{2p^2 t}{\tau_R}\right) \right. \\
 & \left. + \frac{1}{5Z} \sum_{p=1}^{Z-1} \exp\left(-\frac{p^2 t}{\tau_R}\right) + \frac{4}{5} \mu^{\text{LM}}(t) R(t) \right].
 \end{aligned} \tag{18}$$



Here  $G_e = G(\tau_e) = \rho k_B T / N_e$  and  $\mu^{\text{LM}}(t)$  is the surviving tube fraction which is calculated using Eq. (9). The first term of Eq. (18) describes the initial Rouse motion, the second term is the contribution of the relaxation of longitudinal modes (a CLF effect causing redistribution of segments along the tube), and the third term accounts for the contribution of escaping from the tube via  $\mu^{\text{LM}}(t)$  and for the effect of CR via the function  $R(t)$ . This latter function was originally introduced by Rubinstein and Colby [8] within a Rouse-tube model of CR and must be determined self-consistently, assuming that the tube can be modeled as an effective Rouse chain with random bead mobilities whose distribution depends on  $\mu(t)$  in a self-consistent manner. Likhtman and McLeish introduced an additional fitting parameter,  $c_\nu$ , which controls the decay rate of  $R(t)$  and therefore the strength of CR ( $c_\nu = 1$  corresponds to the original Rubinstein and Colby model,  $c_\nu = 0$  to the total neglect of CR). Here we use  $c_\nu = 1$  and determine  $R(t)$  using the algorithm proposed by Rubinstein and Colby [8]. For  $t < \tau_R$ , the functional form of  $R(t)$  is similar to  $\mu^{\text{LM}}(t)$  (Eq. (9)), however, with a different prefactor:  $R(t) = 1 - (1.8/Z)(t/\tau_e)^{1/4}$ . At  $t > \tau_R$ ,  $R(t)$  decays more slowly than  $\mu^{\text{LM}}(t)$  and exhibits a tail. Figure S4 of SI shows  $\mu^{\text{LM}}(t)$  and  $R(t)$  together (for  $Z = 20$ ).

After setting  $c_\nu = 1$ , Eq. (18) has three input parameters:  $N_e$ ,  $\tau_e$ , and  $\tau_R$ .  $\tau_e$  and  $\tau_R$  can be calculated using  $\tau_e = \tau_0 N_e^2$  and  $\tau_R = \tau_0 N^2$  and if  $\tau_0$  is known (for the current model  $\tau_0 = 1.47\tau$ ),  $N_e$  is the only free parameter. Motivated by the discussion above about the value of the plateau modulus we set  $N_e = 52$ . Therefore, there is no adjustable parameter. Fig. 15a shows the prediction of the Likhtman-McLeish model, Eq. (18), for  $G(t)$  at chain lengths  $N = 200$ ,  $N = 400$ , and  $N = 1000$ . Following the trend already observed in  $P(t)$  (Fig. 5), the model does not capture the behavior of  $G(t)$  very well for  $N = 200$ , but the quality of the prediction improves with increasing  $N$ .

To rationalize this behavior, a short discussion about the general behavior of the model is worth mentioning. At late times, Eq. (18) simplifies to  $G(t) = G_0^N \mu(t) R(t)$ . However, recall that at long times, approximately,  $G(t) = G_0^N P(t)^2$  (see Fig. 14). Therefore, the model produces a good prediction of  $G(t)$  when  $\mu^{\text{LM}}(t) R(t)$  is almost equal to  $P(t)^2$ . Furthermore, in the range of chain length studied here,  $R(t)$  is not far from  $\mu^{\text{LM}}(t)$  (see Figure S4), and for the current discussion about the general behavior of the model, it can be roughly estimated with  $\mu^{\text{LM}}(t)$ ; therefore, the prediction of the model is roughly  $G(t) \approx G_0^N \mu^{\text{LM}}(t)^2$ . Hence, the model makes a good prediction when  $\mu^{\text{LM}}(t)$  is close to  $P(t)$ . Consistent with this explanation, the prediction of the model for the  $G(t)$  of  $N = 200$  is not good, because the  $\mu^{\text{LM}}(t)$  does not properly describe the  $P(t)$  of  $N = 200$  (see the discussion of Fig. 5). As mentioned above, in the Likhtman-McLeish model,  $R(t)$  contains a fitting parameter,  $c_\nu$ , which is set to be equal to 1 in the current work. By assuming  $c_\nu$  to be chain length-dependent and using  $c_\nu \ll 1$  for

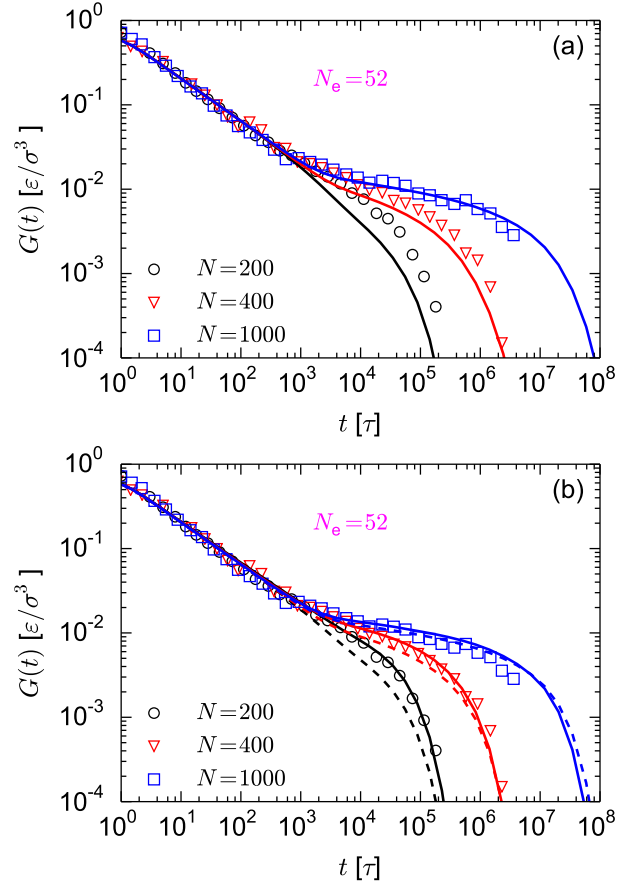


FIG. 15. Simulation data for  $G(t)$  (symbols) for chain lengths  $N = 200$ ,  $N = 400$ , and  $N = 1000$  compared to the predictions of the Likhtman-McLeish model with  $N_e = 52$ . Solid lines in panel (a) show the result of using the original  $R(t)$  function of the model with  $c_\nu = 1$ . Panel (b) shows the results of using the double reptation approximation for CR. In this panel, the dashed lines were calculated assuming  $R(t) = \mu^{\text{LM}}(t)$  with  $\mu^{\text{LM}}(t)$  taken from Eq. (9). The solid lines were calculated by replacing  $\mu(t)R(t)$  in Eq. (18) with  $P(t)^2$ .

$N = 200$  and  $N = 400$ , it is possible to change the decay rate of  $R(t)$  and, consequently, to improve the quality of fitting significantly (Figure S5 shows the output of the model with  $c_\nu = 0.1$ ). However, such a modification only enables the model to fit the simulation results and does not improve its predictive power.

The results presented in Fig. 14 (comparison between  $G(t)$  and  $P(t)^2$ ) suggest taking into account the CR mechanism via the double reptation approximation. In Fig. 15b, the dashed lines show the results of assuming  $R(t) = \mu^{\text{LM}}(t)$ . As mentioned above,  $R(t)$  calculated based on the Rouse-tube model of CR is close to  $\mu^{\text{LM}}(t)$ , but it is not identical to  $\mu^{\text{LM}}(t)$ ; particularly,  $R(t)$  has a long-time tail (see Figure S4). The calculated  $G(t)$  curves based on  $R(t) = \mu^{\text{LM}}(t)$  assumption are also close to those calculated based on the original  $R(t)$  of the model, and the current simulation results are not decisive for comparing the accuracy of these two methods of treating

the CR mechanism. The solid lines in Fig. 15b are also the results of double relation approximation, however, both  $\mu(t)$  and  $R(t)$  are replaced with  $P(t)$  (*i.e.*,  $R(t)\mu(t)$  in Eq. (18) is replaced by  $P(t)^2$  and Eq. (9) has not been used for the calculations). Based on this assumption, good estimates of  $G(t)$  can be provided for all  $N$ , from the short-time Rouse regime up to the terminal time. This is consistent with the results shown in Fig. 14. To show the effect of  $N_e$ , in Figure S6 we also present the results of the replacement  $\mu(t)R(t) \rightarrow P(t)^2$ , but using  $N_e = N_{e,\text{ppa}} = 87$ . Consistent with the trend observed in Fig. 14, the resulting curves deviate significantly from the simulation data.

The above approximation (replacement of  $\mu(t)R(t)$  with  $P(t)^2$ ) is similar in spirit to an approach proposed by Hou *et al.* [37], who replaced  $\mu(t)R(t)$  by  $\mu(t)^2$  in Eq. (18) according to the double reptation approximation and estimated  $\mu(t)$  by simulations from the autocorrelation function of the end-to-end vectors of the primitive chains (chain conformation averaged over a period  $\tau_e$  [86]). Combining this method with the use of  $N_{e,\text{ppa}}$  for the entanglement length, they also obtained excellent agreement between the predicted and measured values of  $G(t)$  for short and mildly entangled chains. However, the results presented in the current work and also the results of Hou *et al.* [37] for long chains, suggest that  $G_{N,\text{ppa}}^0 = 4/5\rho k_B T/N_{e,\text{ppa}}$  underestimates the plateau modulus. Furthermore, by using  $N_e = 52$  we can simplify the overall picture and reveal a simple relation between  $G(t)$  and  $P(t)^2$  even for mildly entangled chains (instead of a relation between  $G(t)$  and end-to-end motion of the primitive chains).

From  $G(t)$ , we can also calculate the storage and loss moduli of oscillatory shear,  $G'(\omega)$  and  $G''(\omega)$ , by Fourier transform. By fitting  $G(t)$  with a series of exponential functions (Maxwell modes), the transformation can be performed analytically [21, 38]: if  $G(t) = \sum_i g_i \exp(-t/\lambda_i)$  then  $G'(\omega) = \sum_i g_i \lambda_i^2 \omega^2 / (1 + \lambda_i^2 \omega^2)$  and  $G''(\omega) = \sum_i g_i \lambda_i \omega / (1 + \lambda_i^2 \omega^2)$ .

Fig. 16 (symbols) show the  $G'(\omega)$  and  $G''(\omega)$  calculated through fitting exponential functions, for  $N = 30$ , 100, and 400, for frequencies smaller than those of the segmental dynamics and bond vibrations. For the fitting, we ignored the short-time oscillations of  $G(t)$  due to bond vibrations and fitted the Maxwell modes in the range  $t > 0.01\tau$ . For comparison, the figure also shows the results obtained by a direct Fourier transform of the bare data using the Reptate package [38, 87] (dashed lines), which agree with the exponential fit data, but are much more noisy in the low-frequency limit. The  $G'(\omega)$  and  $G''(\omega)$  curves feature the signatures of the transition from unentangled to entangled dynamics. For moderately entangled chains with length  $N = 400$ , two crossing points are observed between  $G'(\omega)$  and  $G''(\omega)$ ; also, at frequencies higher than the high-frequency cross-over point  $G''(\omega) > G'(\omega)$ . For  $N = 100$ , the moduli curves are almost tangent, and for  $N = 30$ , the intersection of  $G'(\omega)$  and  $G''(\omega)$  is not observed. The high-frequency

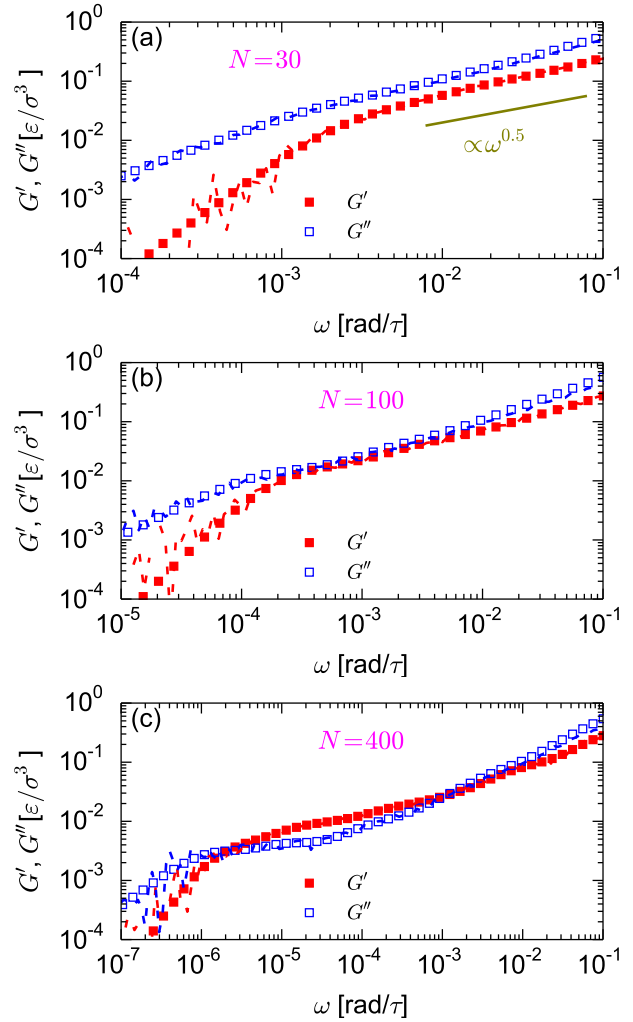


FIG. 16. Storage and loss moduli,  $G'(\omega)$  and  $G''(\omega)$ , for chains of length (a)  $N = 30$ , (b)  $N = 100$ , and (c)  $N = 400$ . The symbols show the moduli calculated by fitting a sum of exponential functions to  $G(t)$ . The dashed lines show the moduli calculated via the direct Fourier transform of  $G(t)$ .

intersection point between  $G'(\omega)$  and  $G''(\omega)$  provides an estimate of  $\tau_e \approx 1/\omega_{\text{cross}}$  [38]. For  $N = 400$ , we obtain  $1/\omega_{\text{cross}} \approx 800\tau$ , which is smaller than other estimates of  $\tau_e$ , including the one based on  $G(\tau_e) = \rho k_B T/N_e$  discussed above.

We note that Likhtman *et al.* [14] performed a similar analysis, also using the Kremer-Grest model, and did not observe a high-frequency intersection between  $G'(\omega)$  and  $G''(\omega)$  for entangled chains. This discrepancy is probably due to differences in the fitting procedures. According to our experience with the Kremer-Grest model and also other atomistic and coarse-grained polymer models [21], the high-frequency cross-over point is observed when time scales smaller than the timescale of segmental dynamics are included in the fitting range (that is, the drop of  $G(t)$  due to segmental dynamics must be included).

We conclude the discussion of the viscoelastic prop-

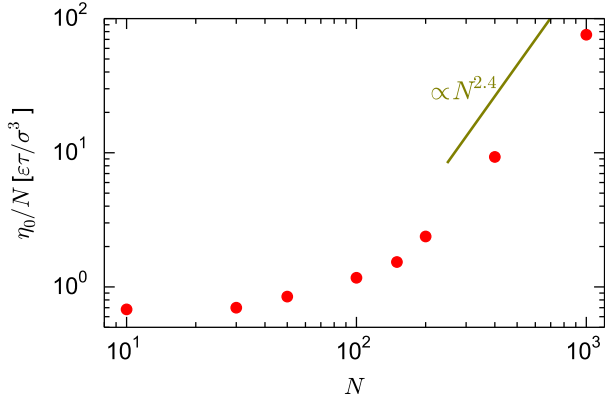


FIG. 17. Zero-shear viscosity divided by chain length,  $\eta_0/N$ , versus  $N$ .

erties by analyzing the zero-shear viscosity, which can be calculated from the integral of  $G(t)$ ,  $\eta_0 = \int_0^\infty G(t)dt$ . The integral was calculated analytically after fitting  $G(t)$  with a series of exponential functions as described above. For the longest chains with  $N = 1000$ , the data for  $G(t)$  do not have good statistics at late times; for this case, the long time behavior of  $G(t)$  was estimated by  $G_N^0 P(t)^2$  (see Fig. 14). Fig. 17 shows  $\eta_0/N$  versus  $N$ . One can clearly see the transition from Rouse behavior ( $\eta_0 \sim N$ ) to the entangled regime. However, in the range of studied chain lengths, a small deviation from the expected scaling exponent  $\approx 3.4$ , which would be consistent with the exponent observed for  $\tau_d$  (Fig. 6), is observed. For very large  $N$ , the contribution of the short-time Rouse dynamics is negligible, and  $\eta_0$  is dominated by the entangled dynamics with a characteristic time of  $\tau_d$ . However, for moderately entangled chains, the contribution of the Rouse regime, which has a  $N$ -independent characteristic time of  $\tau_e$ , can not be ignored. This contribution leads to a deviation of the scaling exponent of  $\eta_0$  from the scaling exponent of  $\tau_d$  for moderately entangled chains.

#### IV. SUMMARY

We have presented a detailed analysis of the relaxation dynamics of linear polymer melts using molecular dynamics simulations. Simulations were performed using the standard Kremer-Grest bead-spring model of chains with different lengths, ranging from  $N = 10$  up to  $N = 1000$ . This latter  $N$  corresponds to  $Z \approx 20$  entanglements per chain based on  $N_e = 52$  as estimated from the plateau modulus. We focused on the analysis of mean-squared displacements ( $g_1(t)$  and  $g_3(t)$ ), the autocorrelation function of the end-to-end vector ( $P(t)$ ), the single-chain dynamic structure factor ( $S(q, t)$ ), and linear viscoelastic properties, particularly the shear stress-relaxation modulus ( $G(t)$ ). Based on the results of the single-chain dynamic structure factor, we also computed wave-vector dependent relaxation rates  $\tau(q)$  and non-local mobility functions,

$\Lambda(q)$ , that can be used in dynamical density functional theory calculations of the dynamics of structure evolution in heterogeneous polymer melts.

Special attention was given to detecting the signs of different relaxation mechanisms of entangled melts, namely CLF (contour length fluctuation), CR (constraint release), and reptation, and to the comparison of the simulation data with analytical theories based on the tube model and on the concept of the “surviving tube fraction”  $\mu(t)$ . Our main results can be summarized as follows:

- With increasing chain length, gradual development of scaling regimes ( $1 - P(t) \sim t^{1/4}$  and  $\chi''(\omega) \sim \omega^{-1/4}$  (where  $\chi''(\omega)$  is dynamic susceptibility and shows end-to-end dynamics on the frequency domain) is observed. These regimes can be explained based on CLF which is responsible for the appearance of a scaling regime ( $1 - \mu(t) \sim t^{1/4}$  at intermediate times. Neglecting the CR effect, we have  $P(t) = \mu(t)$ , and the above scaling regimes are consistent with the expectation based on CLF.
- A general agreement between the time dependence of  $g_1(t)$  and the time dependence of  $(1 - P(t))$  is observed. Particularly, because of the restricted Rouse motion of the chain in their tubes, both quantities scale with  $t^{1/4}$  in the interval of  $\tau_e < t < \tau_R$ .
- We observed signatures of the CR process in the relaxation of  $S(q, t)$  and  $G(t)$ . In the absence of CR, the tube theory predicts  $S(q, t) \propto G(t) \propto P(t) = \mu(t)$  at  $t \gg \tau_e$  and  $2\pi/R_{ee} \ll q \ll 2\pi/a$ . For both  $S(q, t)$  and  $G(t)$ , proportionality with  $P(t)$  was not observed; both quantities decay significantly faster than  $P(t)$ . Instead, we find  $G(t) \propto P(t)^2$ , consistent with the dynamic tube dilation or double reptation approximations.
- One can estimate the plateau modulus and its corresponding entanglement length from the  $G(t)$  data using the following self-consistency condition: for a given  $N_e$  value one can calculate a  $\tau_e$  from the  $G(t)$  curves using  $G(\tau_e) = \rho k_B T / N_e$ ; this  $\tau_e$  value is expected to be consistent with the Rouse time of  $N_e$  monomers, *i.e.*,  $\tau_e = \tau_0 N_e^2$ . In the case of the fully flexible Kremer-Grest polymer melts studied here, we found  $N_e = 52$ , which was previously calculated using an equivalent single-chain slip-link model [14], and is much smaller than the value  $N_{e,ppa} = 87$  obtained by the primitive path analysis, satisfies the above condition.
- The measured  $P(t)$  and  $S(q, t)$  data were compared with the predictions of the pure reptation and the predictions based on CLF and reptation. In both cases, pure reptation does not properly describe the simulation results. In the case of  $P(t)$ , the inclusion of CLF significantly improves the quality of theoretical predictions. However, even the CLF

model did not provide a satisfactory description of the  $S(q, t)$  data. This signals the importance of CR for the relaxation of  $S(q, t)$ , at least in the range of chain lengths studied here.

- The simulation results for  $G(t)$  were compared with the predictions of the Likhtman-McLeish [56] model which takes into account reptation, CLF, and CR mechanisms. The model does not describe the simulation results for mildly entangled chains, however, the quality of the prediction improves with increasing chain length. At late times, the model assumes a simple functions form:  $G(t) = G_N^0 \mu(t) R(t)$ , where  $R(t)$  accounts for the contribution of CR. Motivated by the relation  $G(t) = G_N^0 P(t)^2$  (mentioned above), we replaced  $\mu(t) R(t)$  term in the model with  $P(t)^2$  and obtained excellent agreement between the resulting curves and the simulation data for  $G(t)$ . However, in this case, only the short-time behavior of  $G(t)$  is constructed based on theoretical expressions.

### Supporting Information

The Supporting Information contains: (1) Mean-squared displacements of the centers-of-mass of the chains. (2) Description of  $P(t)$  based on  $N_{e,ppa}$ . (3) Theoretical predictions for the  $S(q, t)$  of  $N = 400$ . (4) Comparing  $R(t)$  and  $\mu(t)$  of the Likhtman-McLeish model. (5) The effect of  $c_\nu$  on the output of the Likhtman-McLeish model. (6) Description of  $G(t)$  based on  $N_{e,ppa}$ .

### Acknowledgements

This research was supported by the German Science Foundation (DFG) via SFB TRR 146 (Grant number 233630050, project C1). The simulations were carried out on the high performance computing center MOGON at JGU Mainz.

### REFERENCES

- [1] Pierre-Giles De Gennes, "Reptation of a polymer chain in the presence of fixed obstacles," *J. Chem. Phys.* **55**, 572–579 (1971).
- [2] Masao Doi, Sam F Edwards, and Samuel Frederick Edwards, *The theory of polymer dynamics*, Vol. 73 (Oxford university press, 1988).
- [3] Michael Rubinstein and Ralph H Colby, *Polymer physics*, Vol. 23 (Oxford university press New York, 2003).
- [4] Tom CB McLeish, "Tube theory of entangled polymer dynamics," *Adv. Phys.* **51**, 1379–1527 (2002).
- [5] Masao Doi, *Introduction to polymer physics* (Oxford university press, 1996).
- [6] Masao Doi, "Explanation for the 3.4-power law for viscosity of polymeric liquids on the basis of the tube model," *J. Polym. Sci., Polym. Phys. Ed.* **21**, 667–684 (1983).
- [7] Michael Rubinstein, Eugene Helfand, and Dale S Pearson, "Theory of polydispersity effects of polymer rheology: binary distribution of molecular weights," *Macromolecules* **20**, 822–829 (1987).
- [8] Michael Rubinstein and Ralph H Colby, "Self-consistent theory of polydisperse entangled polymers: Linear viscoelasticity of binary blends," *J. Chem. Phys.* **89**, 5291–5306 (1988).
- [9] G Marrucci, "Relaxation by reptation and tube enlargement: A model for polydisperse polymers," *J. Polym. Sci., Polym. Phys. Ed.* **23**, 159–177 (1985).
- [10] Hiroshi Watanabe, "Slow dynamics in homopolymer liquids," *Polym. J.* **41**, 929–950 (2009).
- [11] Kurt Kremer and Gary S Grest, "Dynamics of entangled linear polymer melts: A molecular-dynamics simulation," *J. Chem. Phys.* **92**, 5057–5086 (1990).
- [12] Mathias Pütz, Kurt Kremer, and Gary S Grest, "What is the entanglement length in a polymer melt?" *Europhys. Lett.* **49**, 735 (2000).
- [13] Qiang Zhou and Ronald G Larson, "Direct calculation of the tube potential confining entangled polymers," *Macromolecules* **39**, 6737–6743 (2006).
- [14] Alexei E Likhtman, Sathish K Sukumaran, and Jorge Ramirez, "Linear viscoelasticity from molecular dynamics simulation of entangled polymers," *Macromolecules* **40**, 6748–6757 (2007).
- [15] Pavlos S Stephanou, Chunggi Baig, Georgia Tsolou, Vlassis G Mavrantzas, and Martin Kröger, "Quantifying chain reptation in entangled polymer melts: Topological and dynamical mapping of atomistic simulation results onto the tube model," *J. Chem. Phys.* **132** (2010).
- [16] Zuowei Wang, Alexei E Likhtman, and Ronald G Larson, "Segmental dynamics in entangled linear polymer melts," *Macromolecules* **45**, 3557–3570 (2012).
- [17] K Michael Salerno, Anupriya Agrawal, Dvora Perahia, and Gary S Grest, "Resolving dynamic properties of polymers through coarse-grained computational studies," *Phys. Rev. Lett.* **116**, 058302 (2016).
- [18] Hsiao-Ping Hsu and Kurt Kremer, "Static and dynamic properties of large polymer melts in equilibrium," *J. Chem. Phys.* **144** (2016).
- [19] K Kempfer, J Devémy, Alain Dequidt, M Couty, and P Malfreyt, "Realistic coarse-grain model of cis-1, 4-polybutadiene: from chemistry to rheology," *Macromolecules* **52**, 2736–2747 (2019).
- [20] Carsten Svaneborg and Ralf Everaers, "Characteristic time and length scales in melts of kremer–grest bead-spring polymers with wormlike bending stiffness," *Macromolecules* **53**, 1917–1941 (2020).
- [21] Alireza F Behbahani, Ludwig Schneider, Anastassia Rissanou, Anthony Chazirakis, Petra Bacova, Pritam Kumar Jana, Wei Li, Manolis Doxastakis, Patrycja Polinska, Craig Burkhart, *et al.*, "Dynamics and rheology of polymer melts via hierarchical atomistic, coarse-grained, and slip-spring simulations," *Macromolecules* **54**, 2740–2762 (2021).
- [22] Wei Li, Pritam K Jana, Alireza F Behbahani, Georgios Kritikos, Ludwig Schneider, Patrycja Polinska, Craig Burkhart, Vagelis A Harmandaris, Marcus Müller, and Manolis Doxastakis, "Dynamics of long entangled polyisoprene melts via multiscale modeling," *Macromolecules* **54**, 8693–8713 (2021).
- [23] Martin Kröger and Siegfried Hess, "Rheological evidence for a dynamical crossover in polymer melts via nonequi-

- librium molecular dynamics,” *Phys. Rev. Lett.* **85**, 1128 (2000).
- [24] VA Harmandaris, VG Mavrantzas, DN Theodorou, Martin Kröger, J Ramirez, Hans Christian Öttinger, and D Vlassopoulos, “Crossover from the rouse to the entangled polymer melt regime: signals from long, detailed atomistic molecular dynamics simulations, supported by rheological experiments,” *Macromolecules* **36**, 1376–1387 (2003).
- [25] F Lahmar, C Tzoumanekas, Doros N Theodorou, and B Rousseau, “Onset of entanglements revisited. dynamical analysis,” *Macromolecules* **42**, 7485–7494 (2009).
- [26] Sachin Shanbhag and Zuwei Wang, “Molecular simulation of tracer diffusion and self-diffusion in entangled polymers,” *Macromolecules* **53**, 4649–4658 (2020).
- [27] Hsiao-Ping Hsu and Kurt Kremer, “Detailed analysis of rouse mode and dynamic scattering function of highly entangled polymer melts in equilibrium,” *Euro. Phys. J., Spec. Top.* **226**, 693–703 (2017).
- [28] Dieter Richter, Michael Monkenbusch, Arantxa Arbe, and Juan Colmenero, “Neutron spin echo in polymer systems,” *Neutron Spin Echo in Polymer Systems: -/-*, 1–221 (2005).
- [29] BJ Gold, Wim Pyckhout-Hintzen, Andreas Wischnewski, Aurel Radulescu, Michael Monkenbusch, J Allgaier, Ingo Hoffmann, Daniele Parisi, Dimitris Vlassopoulos, and Dieter Richter, “Direct assessment of tube dilation in entangled polymers,” *Phys. Rev. Lett.* **122**, 088001 (2019).
- [30] Michael Monkenbusch, Margarita Kruteva, and Dieter Richter, “Dynamic structure factors of polymer melts as observed by neutron spin echo: Direct comparison and reevaluation,” *J. Chem. Phys.* **159** (2023).
- [31] Margarita Kruteva, Jürgen Allgaier, Michael Monkenbusch, Rustem Valiullin, Ingo Hoffmann, and Dieter Richter, “Cooperative dynamics of highly entangled linear polymers within the entanglement tube,” *ACS Macro Letters* **13**, 335–340 (2024).
- [32] PG De Gennes, “Coherent scattering by one reptating chain,” *Journal de Physique* **42**, 735–740 (1981).
- [33] John D Ferry, *Viscoelastic properties of polymers* (John Wiley & Sons, 1980).
- [34] Ralph H Colby, Lewis J Fetters, and William W Graessley, “The melt viscosity-molecular weight relationship for linear polymers,” *Macromolecules* **20**, 2226–2237 (1987).
- [35] Evelyne Van Ruymbeke, Roland Keunings, Vincent Stéphenne, A Hagenaaers, and Christian Bailly, “Evaluation of reptation models for predicting the linear viscoelastic properties of entangled linear polymers,” *Macromolecules* **35**, 2689–2699 (2002).
- [36] Dietmar Auhl, Jorge Ramirez, Alexei E Likhtman, Pierre Chambon, and Christine Fernyhough, “Linear and non-linear shear flow behavior of monodisperse polyisoprene melts with a large range of molecular weights,” *J. Rheol.* **52**, 801–835 (2008).
- [37] Ji-Xuan Hou, Carsten Svaneborg, Ralf Everaers, and Gary S Grest, “Stress relaxation in entangled polymer melts,” *Phys. Rev. Lett.* **105**, 068301 (2010).
- [38] Manlio Tassieri, Jorge Ramirez, Nikos Ch Karayiannis, Sathish K Sukumaran, and Yuichi Masubuchi, “i-rheo gt: Transforming from time to frequency domain without artifacts,” *Macromolecules* **51**, 5055–5068 (2018).
- [39] Heyi Liang, Kenji Yoshimoto, Masahiro Kitabata, Umi Yamamoto, and Juan J de Pablo, “Multiscale rheology model for entangled nylon 6 melts,” *J. Polym. Sci.* **60**, 3071–3084 (2022).
- [40] Zakiya Shireen, Elnaz Hajizadeh, Peter Daivis, and Christian Brandl, “Linear viscoelastic shear and bulk relaxation moduli in poly (tetramethylene oxide)(ptmo) using united-atom molecular dynamics,” *Comput. Mater. Sci.* **216**, 111824 (2023).
- [41] Hiroshi Watanabe, “Dielectric relaxation of type-a polymers in melts and solutions,” *Macromol. Rapid Commun.* **22**, 127–175 (2001).
- [42] A Abou Elfadl, R Kahlau, A Herrmann, VN Novikov, and EA Rossler, “From rouse to fully established entanglement dynamics: a study of polyisoprene by dielectric spectroscopy,” *Macromolecules* **43**, 3340–3351 (2010).
- [43] T Glomann, GJ Schneider, AR Brás, W Pyckhout-Hintzen, A Wischnewski, R Zorn, J Allgaier, and D Richter, “Unified description of the viscoelastic and dielectric global chain motion in terms of the tube theory,” *Macromolecules* **44**, 7430–7437 (2011).
- [44] Maksim E Shivokhin, Daniel J Read, Dimitris Kouloumasis, Rok Kocen, Flanco Zhuge, Christian Bailly, Nikos Hadjichristidis, and Alexei E Likhtman, “Understanding effect of constraint release environment on end-to-end vector relaxation of linear polymer chains,” *Macromolecules* **50**, 4501–4523 (2017).
- [45] Daniel J Read, Maksim E Shivokhin, and Alexei E Likhtman, “Contour length fluctuations and constraint release in entangled polymers: Slip-spring simulations and their implications for binary blend rheology,” *J. Rheol.* **62**, 1017–1036 (2018).
- [46] Chi C Hua and Jay D Schieber, “Segment connectivity, chain-length breathing, segmental stretch, and constraint release in reptation models. i. theory and single-step strain predictions,” *J. Chem. Phys.* **109**, 10018–10027 (1998).
- [47] Yuichi Masubuchi, Jun-Ichi Takimoto, Kiyohito Koyama, Giovanni Ianniruberto, Giuseppe Marrucci, and Francesco Greco, “Brownian simulations of a network of reptating primitive chains,” *J. Chem. Phys.* **115**, 4387–4394 (2001).
- [48] Alexei E Likhtman, “Single-chain slip-link model of entangled polymers: Simultaneous description of neutron spin-echo, rheology, and diffusion,” *Macromolecules* **38**, 6128–6139 (2005).
- [49] Sathish K Sukumaran and Alexei E Likhtman, “Modeling entangled dynamics: comparison between stochastic single-chain and multichain models,” *Macromolecules* **42**, 4300–4309 (2009).
- [50] Veronica C Chappa, David C Morse, Annette Zippelius, and Marcus Müller, “Translationally invariant slip-spring model for entangled polymer dynamics,” *Phys. Rev. Lett.* **109**, 148302 (2012).
- [51] Takashi Uneyama and Yuichi Masubuchi, “Multi-chain slip-spring model for entangled polymer dynamics,” *J. Chem. Phys.* **137** (2012).
- [52] Michael Langeloth, Yuichi Masubuchi, Michael C Böhm, and Florian Müller-Plathe, “Recovering the reptation dynamics of polymer melts in dissipative particle dynamics simulations via slip-springs,” *J. Chem. Phys.* **138** (2013).
- [53] Abelardo Ramírez-Hernández, Brandon L Peters, Ludwig Schneider, Marat Andreev, Jay D Schieber, Marcus Müller, and Juan J de Pablo, “A multi-chain polymer slip-spring model with fluctuating number of entanglements: Density fluctuations, confinement, and phase separation,” *J. Chem. Phys.* **146** (2017).

- [54] Georgios G Vogiatzis, Grigorios Megariotis, and Doros N Theodorou, "Equation of state based slip spring model for entangled polymer dynamics," *Macromolecules* **50**, 3004–3029 (2017).
- [55] Y Matsumiya, H Watanabe, and K Osaki, "Comparison of dielectric and viscoelastic relaxation functions of cis-polyisoprenes: Test of tube dilation molecular picture," *Macromolecules* **33**, 499–506 (2000).
- [56] Alexei E Likhtman and Tom CB McLeish, "Quantitative theory for linear dynamics of linear entangled polymers," *Macromolecules* **35**, 6332–6343 (2002).
- [57] John D. Weeks, David Chandler, and Hans C. Andersen, "Role of Repulsive Forces in Determining the Equilibrium Structure of Simple Liquids," *J. Phys. Chem.* **54**, 5237–5247 (1971).
- [58] Aidan P Thompson, H Metin Aktulga, Richard Berger, Dan S Bolintineanu, W Michael Brown, Paul S Crozier, Pieter J In't Veld, Axel Kohlmeyer, Stan G Moore, Trung Dac Nguyen, *et al.*, "Lammps-a flexible simulation tool for particle-based materials modeling at the atomic, meso, and continuum scales," *Comput. Phys. Commun.* **271**, 108171 (2022).
- [59] Ying Li, Martin Kröger, and Wing Kam Liu, "Nanoparticle effect on the dynamics of polymer chains and their entanglement network," *Physical review letters* **109**, 118001 (2012).
- [60] Jagannathan T Kalathi, Sanat K Kumar, Michael Rubinstein, and Gary S Grest, "Rouse mode analysis of chain relaxation in homopolymer melts," *Macromolecules* **47**, 6925–6931 (2014).
- [61] Ralf Everaers, Sathish K Sukumaran, Gary S Grest, Carsten Svaneborg, Arvind Sivasubramanian, and Kurt Kremer, "Rheology and microscopic topology of entangled polymeric liquids," *Science* **303**, 823–826 (2004).
- [62] Livia A Moreira, Guojie Zhang, Franziska Müller, Torsten Stuehn, and Kurt Kremer, "Direct equilibration and characterization of polymer melts for computer simulations," *Macromol. Theory Simul.* **24**, 419–431 (2015).
- [63] Robert S Hoy, Katerina Foteinopoulou, and Martin Kröger, "Topological analysis of polymeric melts: Chain-length effects and fast-converging estimators for entanglement length," *Phys. Rev. E* **80**, 031803 (2009).
- [64] Ji-Xuan Hou, "Note: Determine entanglement length through monomer mean-square displacement," *J. Chem. Phys.* **146** (2017).
- [65] Marina Guenza, "Intermolecular effects in the center-of-mass dynamics of unentangled polymer fluids," *Macromolecules* **35**, 2714–2722 (2002).
- [66] Timothy P Lodge, "Reconciliation of the molecular weight dependence of diffusion and viscosity in entangled polymers," *Phys. Rev. Lett.* **83**, 3218 (1999).
- [67] Hui Tao, Timothy P Lodge, and Ernst D Von Meerwall, "Diffusivity and viscosity of concentrated hydrogenated polybutadiene solutions," *Macromolecules* **33**, 1747–1758 (2000).
- [68] AE Likhtman, "1.06-viscoelasticity and molecular rheology," *Polymer science: a comprehensive reference* **1**, 133–79 (2012).
- [69] Diethelm Boese and Friedrich Kremer, "Molecular dynamics in bulk cis-polyisoprene as studied by dielectric spectroscopy," *Macromolecules* **23**, 829–835 (1990).
- [70] Yumi Matsumiya, Kazuki Kumazawa, Masahiro Nagao, Osamu Urakawa, and Hiroshi Watanabe, "Dielectric relaxation of monodisperse linear polyisoprene: Contribution of constraint release," *Macromolecules* **46**, 6067–6080 (2013).
- [71] Ekaterina Pilyugina, Marat Andreev, and Jay D Schieber, "Dielectric relaxation as an independent examination of relaxation mechanisms in entangled polymers using the discrete slip-link model," *Macromolecules* **45**, 5728–5743 (2012).
- [72] Keiichiro Adachi and Tadao Kotaka, "Dielectric normal mode process in undiluted cis-polyisoprene," *Macromolecules* **18**, 466–472 (1985).
- [73] MG Guenza, "Localization of chain dynamics in entangled polymer melts," *Physical Review E* **89**, 052603 (2014).
- [74] Shota Goto, Kang Kim, and Nobuyuki Matubayasi, "Effects of chain length on rouse modes and non-gaussianity in linear and ring polymer melts," *J. Chem. Phys.* **155** (2021).
- [75] A Wischnewski, M Monkenbusch, L Willner, D Richter, AE Likhtman, TCB McLeish, and B Farago, "Molecular observation of contour-length fluctuations limiting topological confinement in polymer melts," *Physical review letters* **88**, 058301 (2002).
- [76] Sriteja Mantha, Shuanhu Qi, and Friederike Schmid, "Bottom-up construction of dynamic density functional theories for inhomogeneous polymer systems from microscopic simulations," *Macromolecules* **53**, 3409–3423 (2020).
- [77] Pierre-Gilles de Gennes, "Dynamics of fluctuations and spinodal decomposition in polymer blends," *J. Chem. Phys.* **72**, 4756–4763 (1980).
- [78] Phillip Pincus, "Dynamics of fluctuations and spinodal decomposition in polymer blends. ii," *J. Chem. Phys.* **75**, 1996–2000 (1981).
- [79] Marcus Müller and Friederike Schmid, "Incorporating fluctuations and dynamics in self-consistent field theories for polymer blends," *Advanced Computer Simulation Approaches for Soft Matter Sciences II*, 1–58 (2005).
- [80] Friederike Schmid and Bing Li, "Dynamic self-consistent field approach for studying kinetic processes in multiblock copolymer melts," *Polymers* **12**, 2205 (2020).
- [81] JP Wittmer, P Beckrich, A Johner, AN Semenov, SP Obukhov, H Meyer, and J Baschnagel, "Why polymer chains in a melt are not random walks," *Europhys. Lett.* **77**, 56003 (2007).
- [82] Jorge Ramírez, Sathish K Sukumaran, Bart Vorselaars, and Alexei E Likhtman, "Efficient on the fly calculation of time correlation functions in computer simulations," *J. Chem. Phys.* **133** (2010).
- [83] Alireza F Behbahani, Petra Bačová, Patrycja Polińska, Craig Burkhart, Manolis Doxastakis, and Vagelis Harmandaris, "Local viscoelastic properties and shear stress propagation in bulk and confined polymer melts and low-molecular weight liquids," *Phys. Rev. Res.* **6**, 023161 (2024).
- [84] J Des Cloizeaux, "Double reptation vs. simple reptation in polymer melts," *Europhys. Lett.* **5**, 437 (1988).
- [85] J Des Cloizeaux, "Relaxation of entangled polymers in melts," *Macromolecules* **23**, 3992–4006 (1990).
- [86] D. J. Read, K. Jagannathan, and A. E. Likhtman, "Entangled polymers: Constraint release, mean paths, and tube bending energy," *Macromolecules* **41**, 6843–6853 (2008).
- [87] Victor AH Boudara, Daniel J Read, and Jorge Ramírez, "Reptate rheology software: Toolkit for the analysis of theories and experiments," *J. Rheol.* **64**, 709–722 (2020).

# Supporting Information: Relaxation Dynamics of Entangled Linear Polymer Melts via Molecular Dynamics Simulations

Alireza F. Behbahani<sup>1,\*</sup> and Friederike Schmid<sup>1,†</sup>

<sup>1</sup>*Institut für Physik, Johannes Gutenberg-Universität Mainz, Staudingerweg 7, D-55099 Mainz, Germany*

Mean-squared displacements of the centers-of-mass of the chains,  $g_3(t)$

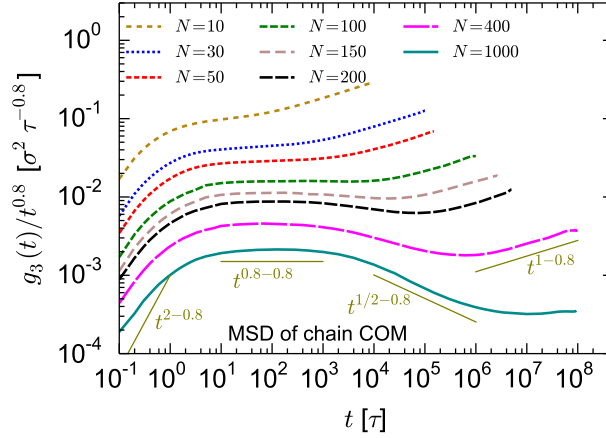


FIG. S1: Mean-squared displacement of the centers-of-mass of the chains divided by  $t^{0.8}$ .

Figure S1 shows  $g_3(t)$  divided by  $t^{0.8}$  for different chain lengths. After the very short time ballistic regime,  $g_3(t)$  of all chains scale almost with  $t^{0.8}$ . This is reflected in the appearance of a short-time plateau regime in the  $g_3(t)/t^{0.8}$  curve. After this regime,  $g_3(t)/t^{0.8}$  of entangled chains ( $N > 100$ ), exhibit a negative slope. With increasing  $N$ , the negative slope tends to the prediction of the tube model ( $g_3(t) \sim t^{0.5}$  or  $g_3(t)/t^{0.8} \sim t^{-0.3}$ ).

## Description of $P(t)$ based on $N_{e,ppa}$

The symbols in Figure S2 show the autocorrelation function of the end-to-end vector,  $P(t)$ , for  $N = 200, 400$ , and  $1000$ . The solid lines show the result of the Likhtman-McLeish model [S1] ( $\mu^{LM}(t)$ , Equation 9 of the main text) using  $N_e = N_{e,ppa} = 87$ . As Figure S2 shows, using  $N_{e,ppa}$  does not lead to a good description of the measured  $P(t)$  data, as compared to the results of using  $N_e = 52$  shown in Figure 5 of the main text.

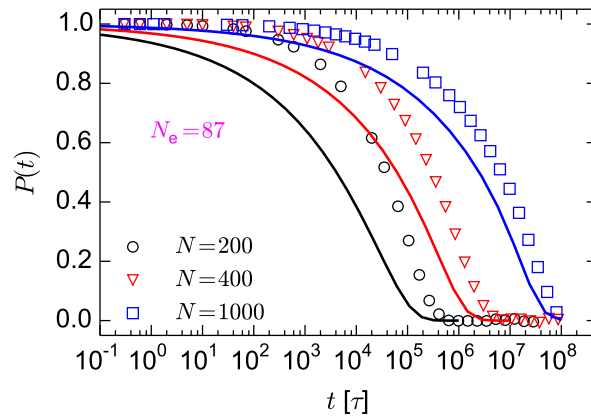


FIG. S2:  $P(t)$  for  $N = 200, 400$ , and  $1000$  (symbols) together with the  $\mu(t)$  of Likhtman-McLeish model (solid lines) with  $N_{e,ppa} = 87$ .

\* aforooza@uni-mainz.de

† friederike.schmid@uni-mainz.de

### Theoretical predictions for the $S(q, t)$ of $N = 400$

Figure S3 shows the the measured  $S(q, t)$  for  $N = 400$ , together with the predictions based on the pure reptation and CLF (contour length fluctuation) processes. Similar to the trend observed for  $N = 1000$  (Figure 11 of the main text), the CLF model describes the  $S(q, t)$  data better and with a smaller apparent entanglement length compared to the pure reptation model.

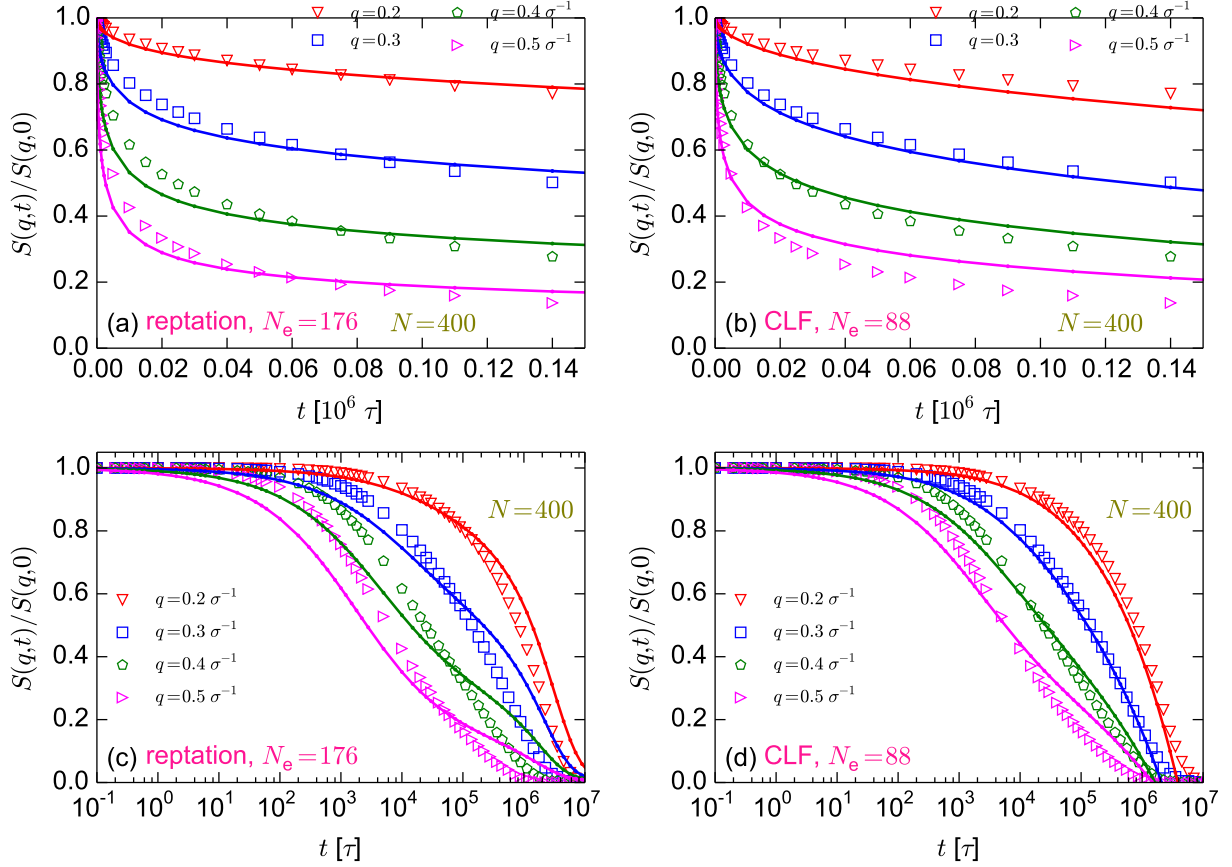


FIG. S3: The symbols show the simulation results for  $S(q, t)/S(q, 0)$  of  $N = 400$  for different values of  $q$ . Solid lines in panels (a) and (c) show the theoretical predictions for  $S(q, t)/S(q, 0)$  based on the pure reptation model with  $N_e = 176$ , in linear and semi-logarithmic scales. Panels (b) and (d) show the theoretical predictions based on CLF with  $N_e = 88$ .



### Comparing $R(t)$ and $\mu(t)$ of the Likhtman-McLeish model

Figure S4 shows the  $\mu(t)$  and  $R(t)$  functions of the Likhtman-McLeish model [S1] for  $Z = N/N_e = 20$ .  $R(t)$  is calculated based on an algorithm proposed by Rubinstein and Colby [S2] based on a Rouse-tube model of CR ( $c_\nu = 1$ ). At  $t > \tau_R$ ,  $R(t)$  decays slower than  $\mu(t)$  and exhibits a tail.

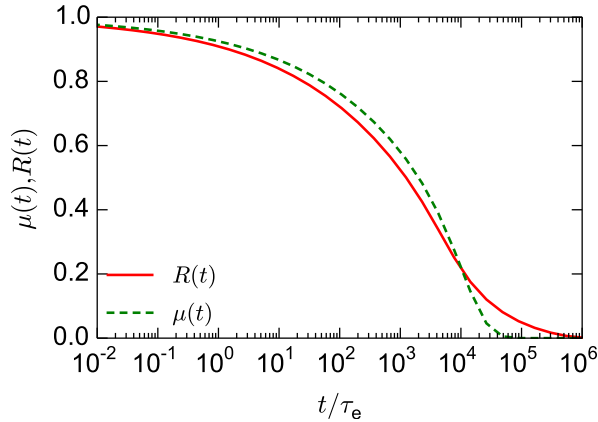


FIG. S4:  $R(t)$  and  $\mu(t)$  of the Likhtman-McLeish model for  $Z = N/N_e = 20$ .

### The effect of $c_\nu$ on the output of the Likhtman-McLeish model

Figure S5 shows the prediction of the Likhtman-McLeish model [S1] with  $c_\nu = 0.1$  together with the prediction obtained by replacing the  $\mu(t)R(t)$  term in the model by  $P(t)^2$ . At long times the Likhtman-McLeish model has a simple functional form:  $G(t) = G_N^0 \mu(t)R(t)$ . One can adjust the decay rate of  $R(t)$  by changing an adjustable parameter,  $c_\nu$ , and as a result, change the resulting  $G(t)$  function.

For  $N = 1000$ ,  $c_\nu = 1$  seems to produce a reasonable prediction (see Figure 15 of the main manuscript). However, with  $c_\nu = 0.1$ , the predicted  $G(t)$  for  $N = 1000$  is slower than expected (that is  $G(t)$  is slower than  $G_N^0 P(t)^2$ ; see Figure 14 of the main manuscript). For  $N = 400$  and  $N = 200$ , the predictions based on  $c_\nu = 0.1$  are better than those with  $c_\nu = 1$ , shown in Figure 15 of the main manuscript. For these chain lengths,  $\mu(t)$  of the Likhtman-McLeish model is faster than the corresponding  $P(t)$  curves (Figure 5 of the manuscript); to compensate for the faster decay of  $\mu(t)$ , we need  $c_\nu \ll 1$  to reduce the decay rate of  $R(t)$  and make  $\mu(t)R(t)$  comparable to  $P(t)^2$  and therefore produce good predictions for  $G(t)$ .

Overall, by assuming  $c_\nu$  to be chain length-dependent it is possible to change the behavior of  $R(t)$  and, consequently, to improve the quality of fitting. However, such a modification only enables the model to fit the simulation results and does not improve its predictive power.

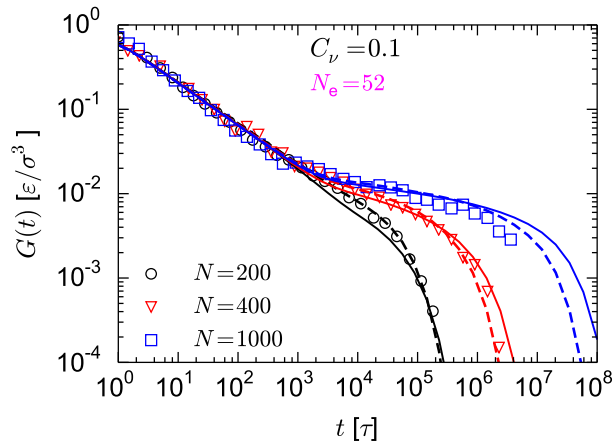


FIG. S5: Symbols: the simulation results for the  $G(t)$  of  $N = 200$ ,  $N = 400$ , and  $N = 1000$ . Solid line: the prediction of the Likhtman-McLeish model with  $N_e = 52$  and  $c_\nu = 0.1$ . Dashed lines: the prediction based on replacing  $\mu(t)R(t)$  by  $P(t)^2$  in the Likhtman-McLeish model.

## Description of $G(t)$ based on $N_{e,\text{ppa}}$

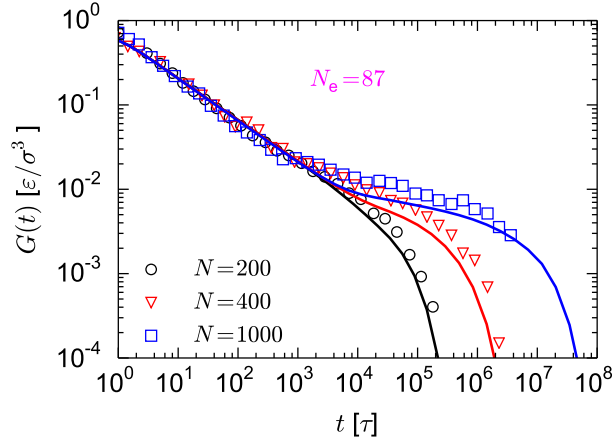


FIG. S6: The simulation results (symbols) for the  $G(t)$  of  $N = 200$ ,  $N = 400$ , and  $N = 1000$  together with theoretical estimations (solid lines) by assuming that the plateau modulus can be calculated based on  $N_{e,\text{ppa}} = 87$ . The solid lines have been calculated based on the Likhtman-McLeish model and double reptation approximation for CR,  $R(t) = \mu(t) = P(t)$ , where  $P(t)$  is the autocorrelation function of the end-to-end vector.

Solid lines in Figure S6 show the the  $G(t)$  curves calculated for  $N = 200$ ,  $N = 400$ , and  $N = 1000$  by assuming that the entanglement length is equal to  $N_{e,\text{ppa}} = 87$ . For the calculation of the solid lines, the  $\mu(t)R(t)$  term in the Likhtman-McLeish model [S1] (Equation 18 of the main text) was replaced with  $P(t)^2$  (see the discussion of Figure 15 of the main text). As can be seen from Figure S6, the  $G(t)$  curves estimated based on  $N_{e,\text{ppa}} = 87$  do not agree with the measured  $G(t)$  data (shown with symbols).

- 
- (S1) Alexei E Likhtman and Tom CB McLeish, “Quantitative theory for linear dynamics of linear entangled polymers,” *Macromolecules* **35**, 6332–6343 (2002).  
(S2) Michael Rubinstein and Ralph H Colby, “Self-consistent theory of polydisperse entangled polymers: Linear viscoelasticity of binary blends,” *J. Chem. Phys.* **89**, 5291–5306 (1988).